TECHNISCHE UNIVERSITÄT MÜNCHEN

Fakultät für Medizin

Advances in Translational Optoacoustics: From Vascular to Vasometabolic Imaging

Angelos Karlas

Vollständiger Abdruck der von der Fakultät für Medizin der Technischen Universität München zur Erlangung des akademischen Grades eines Doktors der Naturwissenschaften genehmigten Dissertation.

Vorsitz: Prof. Dr. Dr. Stefan Engelhardt

Prüfer*innen der Dissertation:

1. Prof. Dr. Vasilis Ntziachristos
2. Prof. Dr. Martin Hrabě de Angelis
3. Prof. Dr. René Botnar

Die Dissertation wurde am 08.06.2020 bei der Technischen Universität München eingereicht und durch die Fakultät für Medizin am 13.04.2021 angenommen.

Advances in Translational Optoacoustics: From Vascular to Vasometabolic Imaging

Angelos Karlas

Supervisor
Prof. V. Ntziachristos

"A thesis submitted in partial fulfilment of the requirements for the degree of Dr.rer.nat. in Experimental Medicine"

Technical University of Munich

2020

ACKNOWLEDGEMENTS

Anyone who started a sentence with “you cannot”.

Anyone who made me change my way of thinking.

Anyone who heard my concerns.

Anyone who managed to maintain his love of honor or “philotimo”.

Angelos Karlas

“Reach what you cannot”
— Nikos Kazantzakis, *Report to Greco*

TABLE OF CONTENTS

ABBREVIATIONS

	Description
AC	Alternating Current
AFG	Arbitrary Function Generator
AMP	Amplifier
BAT	Brown Adipose Tissue
BD	Baseline Diameter
BF	Brightfield
BS	Beamsplitter
CAE	Carotid Thrombendarteriectomy
CCD	Charge-coupled Device
CD	Cross-Sectional Distensibility
CEUS	Contrast-Enhanced Ultrasound
CMR	Continuous Multirecord
CT	Computed Tomography
CTA	Computed Tomography Angiography
DAQ	Data Acquisition Card
DC	Direct Current
DOT	Diffuse Optical Tomography
EA	Cross-Sectional Area
FDG	Fludeoxyglucose
FIR	Far Infrared
FM	Flippable Mirror
FMD	Flow-Mediated Dilatation
fMRI	Functional Magnetic Resonance Imaging
FMT	Fluorescence Molecular Tomography
FOV	Field of View
GM	Galvanometric Mirror
Hb	Deoxygenated Hemoglobin
HbO_2	Oxygenated Hemoglobin
HD	Hyperemia Diameter
HE	Hemalaun-Eosin
ICG	Indocyanine Green
IPH	Intraplaque Hemorrhage
IVUS	Intravascular Ultrasound
LDL	Low Density Lipoprotein
LP-DM	Longpass Dichroic Mirror
MAP	Maximum Amplitude Projection
MPM	Multiphoton Microscopy
MPOM	Multiphoton and Optoacoustic Microscopy
MRI	Magnetic Resonance Imaging
MSOT	Multispectral Optoacoustic Tomography
NADH	Nicotinamide Adenine Dinucleotide
ND	Neutral Density Filter
NIR	Near-Infrared

NLO	Non-Linear Optical
OA	Optoacoustics
OAM	Optoacoustic Microscopy
OL	Objective Lens
PD	Photodiode
PET	Positron Emission Tomography
PMT	Photomultiplier Tube
PSR	Picro-Sirius Red
PWV	Pulse Wave Velocity
RBC	Red Blood Cells
ROI	Region of Interest
RSOM	Raster-Scan Optoacoustic Microscopy
SHG	Second Harmonic Generation
SMC	Smooth Muscle Cells
SP-DM	Shortpass Dichroic Mirror
SPPF	Single-Pulse-Per-Frame
SWIR	Short-Wavelength Infrared
TBV	Total Blood Volume
THG	Third Harmonic Generation
TPEF	Two-Photon Excitation Fluorescence
US	Ultrasound
UT	Ultrasound Transducer
WAT	White Adipose Tissue
WS	Wall Stress

LIST OF FIGURES

ABSTRACT

Vascular imaging may well visualize local pathology, such as stenosis that affects the vessel wall structure and local blood flow but provides no insights into subsequent metabolic dysfunction of the targeted perfused tissue. The latter is monitored by means of functional imaging techniques (e.g. CEUS, fMRI) which visualize tissue perfusion and metabolism and measure tissue function in health and disease. Nevertheless, current such techniques may require the administration of potentially toxic contrast agents (e.g. PET) or the use of bulky and expensive equipment (e.g. fMRI). Optoacoustic imaging, a novel molecular imaging technique, offers label-free imaging of both local vascular pathology and targeted tissue metabolic status with high portability based only upon hemoglobin gradients. We present herein various preclinical and clinical applications of optoacoustic imaging technologies demonstrating the unique potential of optoacoustics to perform vasometabolic imaging of both vascular and tissue pathophysiology providing a more comprehensive view of disease.

Die vaskuläre Bildgebung kann zwar lokale Pathologien wie Stenosen, die die Gefäßwandstruktur und den lokalen Blutfluss beeinflussen, gut sichtbar machen, gibt aber keinen Aufschluss über eine Stoffwechselstörung des durchbluteten Gewebes. Letzteres wird mit Hilfe funktioneller Bildgebungsverfahren (z.B. CEUS, fMRI) evaluiert, die die Gewebedurchblutung und den Stoffwechsel visualisieren und die Gewebefunktion messen. Allerdings erfordern solche Bildgebungsverfahren derzeit möglicherweise die Verabreichung potenziell toxischer Kontrastmittel (z.B. PET) oder die Verwendung sperriger und teurer Geräte (z.B. fMRT). Die Optoakustik, ein neuartiges molekulares Bildgebungsverfahren, bietet eine markierungsfreie und tragbare Darstellung sowohl der lokalen Gefäßpathologie als auch des Gewebestoffwechsels, die nur auf Hämoglobin-Gradienten basiert. Wir präsentieren hier verschiedene präklinische und klinische Anwendungen, die das einzigartige Potenzial der Optoakustik zur Durchführung vasometabolischer Bildgebung sowohl der vaskulären als auch der Gewebepathophysiologie demonstrieren und so einen umfassenderen Überblick über die Krankheit ermöglichen.

Contact details:

Angelos Karlas, MD, Dipl-Ing (MEng), MSc, MRes, DIC
e-mail: angelos.karlas@tum.de

1 Vasometabolic Imaging with Light and Sound: The Unique Opportunity of Optoacoustics

1.1 Translational light-based imaging: A very short introduction

Technological advances in the last decades boosted the translatability of light-based (optical and optoacoustic) imaging from biological samples and small animals to humans. Thus, several optical and optoacoustic imaging techniques have been implemented in both preclinical and clinical platforms so far, offering the opportunity to image excised samples, preclinical models of human disease as well as real patients employing the same imaging technology and further bridging the gap between preclinical research and clinical diagnostic imaging [1].

Optical translational imaging is mainly represented by fluorescence-based techniques where an injected contrast-agent tags a specific molecule under investigation, gets excited by the illumination light of one wavelength (frequency) and emits light of a higher wavelength (lower frequency). Applications range from visualizing cancer [2, 3] to cardiovascular [4, 5] and metabolic imaging [6, 7]. Despite the fact that numerous fluorescence contrast agents developed and introduced in preclinical studies [8], only a small number of contrast agents have been approved for human use. For example, indocyanine green or ICG, a near-infrared dye, which accumulates in the vascular bed as well as in the macrophages and the fluorescein, a green fluorescent dye, which is widely used in the field of ophthalmology to diagnose corneal pathology [9]. ICG has been already used in several clinical applications, such as in peripheral arterial disease [10], cardiac surgical operations [11] and endovascular imaging of inflamed plaques and stents [5].

Nevertheless, light tissue interactions (e.g. photon scattering) radically limit the achieved resolution and contrast of abovementioned techniques for depths higher than the ballistic or unscattered limit of approximately 1 mm. To overcome this limitation several tomographic

optical imaging techniques, such as the fluorescence molecular tomography (FMT) and the diffuse optical tomography (DOT) have been developed. These techniques take advantage of the diffusive photons to provide tomographic images of whole animals, organs or parts of the human body [12-14]. FMT requires the injection of a fluorescent contrast agent while DOT technology can visualize the spatial distributions of oxygenated (HbO_2) and deoxygenated (Hb) hemoglobin revealing functional and metabolic information deep in tissue in vivo without the need for exogenous labels. However, due to light scattering phenomena, both techniques suffer from low spatial resolution of one to several millimetres, and even if they offer excellent optical contrast [14] they are not widely used in the clinics.

Optoacoustic imaging, based on its hybrid nature, attempts to address several limitations of purely optical imaging techniques. By sensing ultrasound waves carrying information about light absorption, optoacoustics provides images with high acoustic resolution as well as high optical contrast, reaching unprecedented imaging depths of several centimetres compared to optical techniques [15] with or without the use of injected contrast agents. This unique opportunity offered by optoacoustic imaging has been substantiated via the development of numerous versatile preclinical and clinical platforms used for a wide range of biomedical applications ranging from cancer [16], to cardiovascular [17] and metabolic field [18]. Herein, we aim at giving a comprehensive description of optoacoustic imaging technology and focusing on vasometabolic imaging applications while sketching the challenges but also the huge scientific interest in achieving the its translation from the laboratory in the clinical setting.

1.2 The optoacoustic or photoacoustic effect

All optoacoustic imaging technologies rely on the same physical principle: The generation of mechanical pressure waves upon the absorption of electromagnetic radiation within a continuum, which is known as the optoacoustic or photoacoustic effect (Fig. 1.1). Nowadays, most of the biomedical optoacoustic systems utilize the visible and near-visible light spectral regions to produce acoustic waves in the region of ultrasound [19]. The energy carried by light

radiation is deposited in the targeted material, depending mainly on its absorption spectrum, and transformed into heat. The resulting increase in temperature causes thermal expansion, which stretches the material and produces mechanical micro-deformations and stress. The pressure waves arising propagate in all directions through the illuminated mass carrying information about the optical properties of the scanned object, as well as, its biomechanical features. In order to give rise to the optoacoustic effect, the light amplitude should fluctuate over time, either continuously (periodically modulated continuous-wave light) or discretely (pulsed light). The spectral characteristics of the thermoelastically-induced pressure waves depend upon the properties of the incident light radiation. Thus, taking into account that modern optoacoustic systems usually use ultrafast lasers (pulses of nano- to femto-second duration), the frequency content of the produced sound waves lies in the ultrasound region.

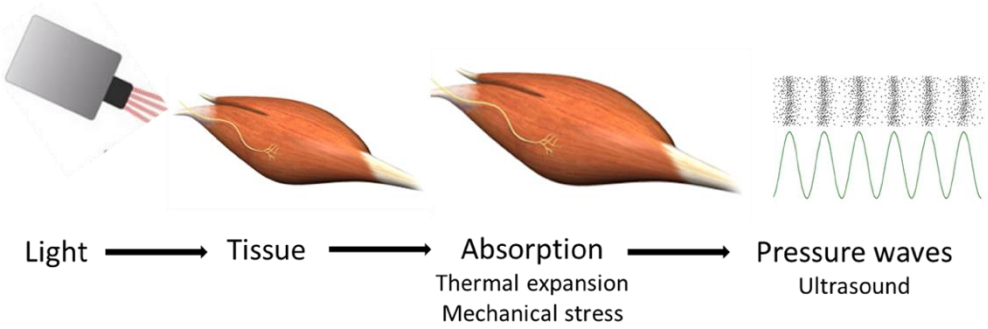

Fig. 1.1. The optoacoustic or photoacoustic effect. Tissue illumination with pulsed light leads to the absorption of light by specific endogenous (e.g. hemoglobins, fat, water) or exogenous (e.g. injected dyes) molecular chromophores. Upon light absorption, tissue thermoelastic expansion and, thus, local mechanical stress is produced due to a minimal increase in local temperature. Finally, these minimal and fast mechanical deformations give rise to mechanical pressure waves, which usually lie in the region of ultrasound.

The basic wave equation ruling the production of optoacoustic waves upon tissue illumination has the following form (Eq. 1.1):

$$\left(\frac{1}{v_{ac}}\frac{\partial^2}{\partial t^2}-\nabla^2\right)P=\frac{\beta}{C_p}\frac{\partial}{\partial t}(\alpha I(\alpha)) \qquad \text{Eq. 1.1}$$

where P is the pressure of the produced optoacoustic wave, v_{ac} is the propagation speed of sound in tissue, β is the coefficient of volumetric thermal expansion, which expresses the changes induced tissue volume change due to a local temperature change, C_p is the thermal energy required to produce the expected local temperature change and $\alpha I(\alpha)$, where α is the light absorption coefficient expressed in cm^{-1}, is a factor reflecting the absorption of light while propagating in biological tissue.

1.3 Optoacoustic systems and platforms for biomedical imaging

Nowadays, there is a wide variety of optoacoustic systems employed for biomedical imaging applications, which may be well classified according to the spatial resolution and the imaging depth achieved [17, 20]. Thus, there are microscopic (few um resolution and less than 1 mm imaging depth), mesoscopic (few tens of um resolution and imaging depth between 1 and 5 mm) and macroscopic systems (few tens to hundreds of um resolution and more than 5 mm penetration depth). This versatility offers a unique opportunity: the use of the same principle in order to conduct molecular imaging of anatomy and biological processes in three different scales: microscopic, mesoscopic and macroscopic.

Numerous customized optoacoustic microscopy (OAM) systems have been developed and used for ex-vivo imaging of cell cultures, engineered tissues and organelles, histological preparations, fresh biological samples or in-vivo imaging of biological processes in small animal models. The resolution of OAM can reach the level of less than 1 um visualizing the microvessels (< 150 um in diameter) in tumors and the mouse brain, as well as, the microarchitecture of the mouse heart or the human carotid atherosclerotic plaque [21-24]. Furthermore, OAM can be combined with other microscopic imaging techniques (please see Chapter 3) in hybrid and multimodality systems to provide complementary molecular information and possibly reveal interactions between different biological processes [24].

Raster-Scan Optoacoustic Mesoscopy (RSOM) is currently the main representative of optoacoustic mesoscopic techniques. By offering excellent spatial resolution of about 7 um,

RSOM has been already used in various biomedical applications, such as skin microvascular imaging in health and in chronic inflammatory skin diseases (e.g. psoriasis) [25, 26]. The technology employs ultra-wideband transducers for ultrasound sensing and usually monochromatic illumination sources (e.g. green light) to provide comprehensive volumetric images of tissue microvasculature at depths of 1 mm. RSOM technology has been employed in both preclinical and clinical applications. During an RSOM measurement raw data is acquired by raster-scanning a skin region (usually 2 x 4 mm) by mechanically moving both the illumination source and the ultrasound transducer over the examined area (usually at steps of 10 μm) and recording ultrasound signals over several predefined measurement positions (one light pulse per signal). The final image is produced by means of tailored reconstruction algorithms that use the signals recorded as input to produce a volumetric image of the scanned region.

Correspondingly, the main representative of macroscopic optoacoustic imaging techniques is the multispectral optoacoustic tomography (MSOT). MSOT principle of operation and technology are thoroughly described later in the current study (please see Section 1.4).

Moreover, apart from the abovementioned non-invasive clinical optoacoustic imaging techniques, catheter-based optoacoustic imaging has been recently introduced for endovascular molecular imaging of atherosclerosis. Various different endovascular optoacoustic systems have been presented so far in efforts to achieve high-resolution atherosclerosis imaging while maintaining small sizes (< 1 mm) enabling imaging even in the coronary arteries. In [27] a resolution of almost 50 um was achieved by using an ultrasound transducer with 45 MHz central frequency, will in the same intravascular ultrasound (IVUS) transducer was employed for both ultrasound and optoacoustic imaging [28]. Endovascular optoacoustic imaging can reveal the lipid, water and collagen content within the subendothelial zone of the arterial wall [29]. Thus, modern catheter-based optoacoustic systems demonstrate great potential for providing comprehensive information about plaque consistency and potentially for detecting or defining novel image-based biomarkers of atherosclerosis [30].

1.4 MSOT technology and dimensions

Multispectral Optoacoustic Tomography (MSOT) is a macroscopic optoacoustic technology used for biomedical imaging and is the one which is more closely to its clinical translation compared to the other optoacoustic imaging technologies. MSOT has been implemented in several different platforms, both preclinical and clinical, opening up great possibilities for the conduction of translational studies.

Modern clinical systems are equipped with hand-held scanning probes with embedded illumination sources and ultrasound detector arrays of hundreds of piezoelectric elements (e.g. n = 256 or 512). Hand-held probes may come in various configurations, either two-dimensional arc-shaped (usually covering an angle of ≈140-170°) or three-dimensional hemisphere-shaped that facilitate the examination of different body regions. Current preclinical systems are characterized by ring-shaped configurations allowing for the whole-volume examination of biological samples or small animals. Due to high spatial (down to 50μm for preclinical setups and approximately 200μm for clinical systems) and temporal resolution (up to 50Hz) [31], the method offers an opportunity to visualize large and small vessels within the same plane, as well as, the potential to monitor changes in the level of tissue perfusion and oxygenation at depths of ≈2-4 cm [32]. Furthermore, modern systems are equipped with traditional ultrasound for extra anatomic orientation.

The multispectral nature of MSOT (transmitting sequences of light pulses with different wavelengths, see Section 1.5 for more details), enables the simultaneous extraction of information about multiple different chromophores, either intrinsic (e.g. oxy- and deoxygenated hemoglobin) or extrinsic (e.g. injected optical contrast agents targeting inflammation). This way, valuable interactions between anatomy and physiology or among different biological processes could be further investigated and revealed.

Thus, MSOT provides the potential to [17, 33]: 1. Visualize both static and dynamic morphology (kinematics) of large vessels, 2. Monitor the microvascular status and blood volume of a whole region, 3. Assess and quantify deep tissue perfusion and oxygenation

dynamics, and 4. Provide co-registered biological and physiological information (after molecular optical labeling). The abovementioned characteristics render MSOT an emerging powerful tool for vascular and metabolic imaging. To this end, apart from providing a comprehensive description of the existing techniques, we introduce and propose MSOT as a new method for assessing endothelial function. MSOT may not simply provide an alternative to the existing platforms but an enhanced tool by integrating multiscale structural, dynamic and biological imaging in a single test.

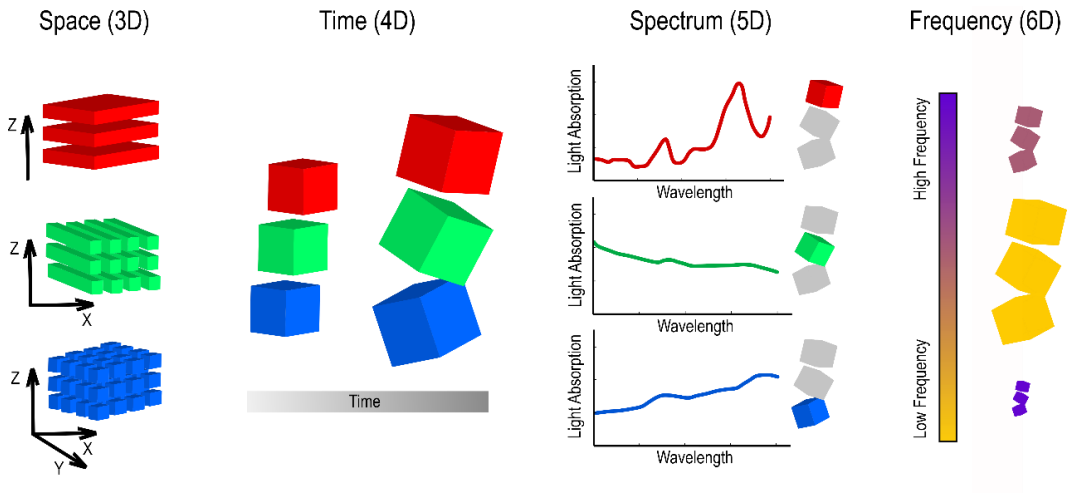

Fig. 1.2. The dimensions imaged by using MSOT. MSOT can provide high resolution (50-200 um) tomographic images of living tissue with a field of view of several centimeters (e.g. 4 x 4 cm) across all spatial dimensions (XYZ, 3D). An imaging framerate of up to 50 Hz allows for real time (4D) tomographic imaging. The spectral dimension (5D) reflects molecular information arising from the spectral signatures of the light-absorbing chromophores. Finally, the potential to visualize many different scales (frequency bands) of structural information in single tomographic image provides an extra option for data visualization (6D).

MSOT revolutionized the field of molecular imaging through its multiscale and multidimensional nature (Fig. 1.2). Apart from the three spatial dimensions (3D) and time (4D), MSOT captures optical spectral data of the scanned objects (5D). Furthermore, an additional frequency domain analysis may provide advanced visualizations of different relative sizes of the imaged objects (6D). Specifically, in the spatial domain, MSOT enables

the extraction of information about many different scales or orders of magnitude while preserving its robustness in the temporal and spectral domains. MSOT produces tomographic images of the illuminated volume reaching a penetration depth of up to several centimeters, overcoming one of the main limitations of all optical imaging techniques.

1.5 MSOT principle of operation

MSOT imaging is based on the optoacoustic effect, where series of light pulses of specific wavelengths (colors) are absorbed by tissue giving rise to ultrasound waves (via thermoelastic expansion, as described in Section 1.2), which are detected by ultrasound detectors and reconstructed into planar images. For each light pulse emitted and absorbed, a tomographic image is produced (single-pulse per frame or SPPF operation, Fig. 1.3).

As a first step during MSOT image acquisition, the ultrasonic detectors (configured in an array, see Section 1.4) record the produced ultrasound waves for each illumination pulse and translate them into voltage recordings. Each ultrasound sensor records a different signal or else a different 'ultrasonic view' of light absorption within the tissue area under examination, so that a set of hundreds (same of number of ultrasound detectors) signals is produced for each illumination pulse.

Finally, for every set of recorded signals a tomographic image is produced by a dedicated image reconstruction algorithm. The algorithm takes into consideration, apart from the recorded signals, the geometry and technical specifications of the used scanning probe. Even if numerous such algorithms have been developed so far, two reconstruction approaches are mainly used for preclinical and clinical MSOT imaging: the back-projection and the model-based approach [19]. After reconstructing the recorded signals, a planar MSOT image for each illumination pulse or wavelength is produced.

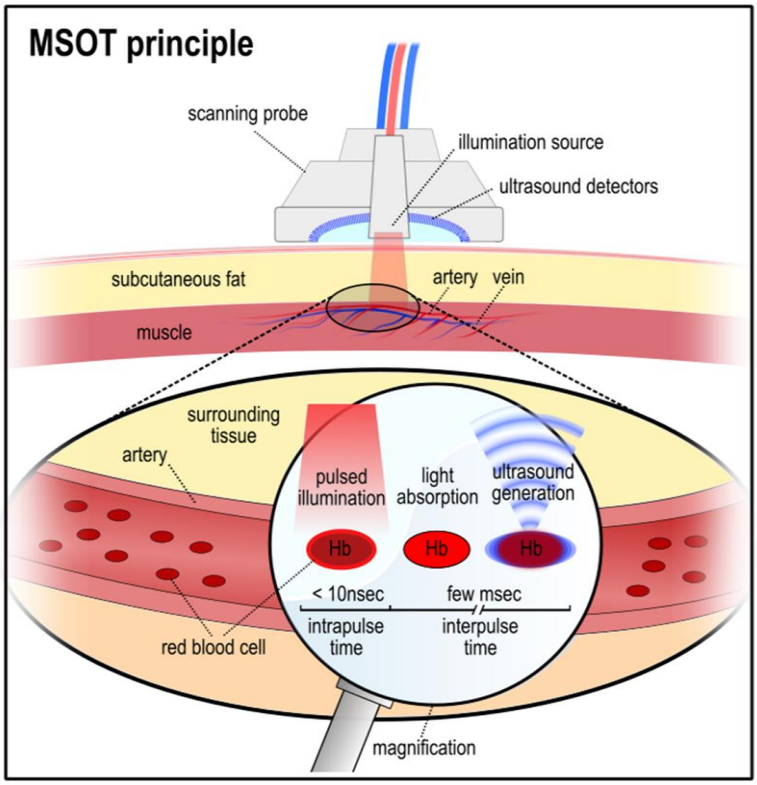

Fig. 1.3. Principle of operation of hand-held MSOT. The emitted light pulses are absorbed by the HbO_2 and Hb in the illuminated arteries and veins correspondingly. Each light pulse (< 10 nsec in duration) gives rise to ultrasound waves via thermoelastic expansion (few msec in duration) which are finally collected by a series of piezoelectric sensors (e.g. n = 256) mount on the same scanning probe. The recorded signals of the piezoelectric sensors are finally reconstructed into tomographic images in accordance to the SPPF principle of operation.

The sequence of the selected illumination wavelengths (e.g. 28 wavelengths from 700 to 970 nm at steps of 10 nm) is periodically repeated during the duration of each MSOT scan, which may widely vary depending on the application. Thus, for each 'period' or group of illumination wavelengths a group of single-wavelength images, or else a 'multispectral stack', is produced (Fig. 1.4). The produced multispectral stack, which may have duration of more than one second for usual frame rates of 25 Hz of modern clinical systems, is used as an input for the spectral unmixing step.

At this step, a set of known chromophore absorption spectra (e.g. HbO_2, Hb, lipid and water) is used as a reference in order to 'spectrally unmix' the recorded multispectral image stack. The spectral unmixing step happens in a per-pixel basis so that the optoacoustically measured

absorption spectrum, or else the representation of the absorption intensity fluctuation of each pixel for all wavelengths across the multispectral stack, is finally 'decomposed' into combinations of the main known spectra. Thus, a new series of unmixed images is produced (e.g. four for the four different chromophores mentioned above) where the intensity of a pixel depends in each unmixed image upon the contribution of a known spectrum in the finally measured spectrum.

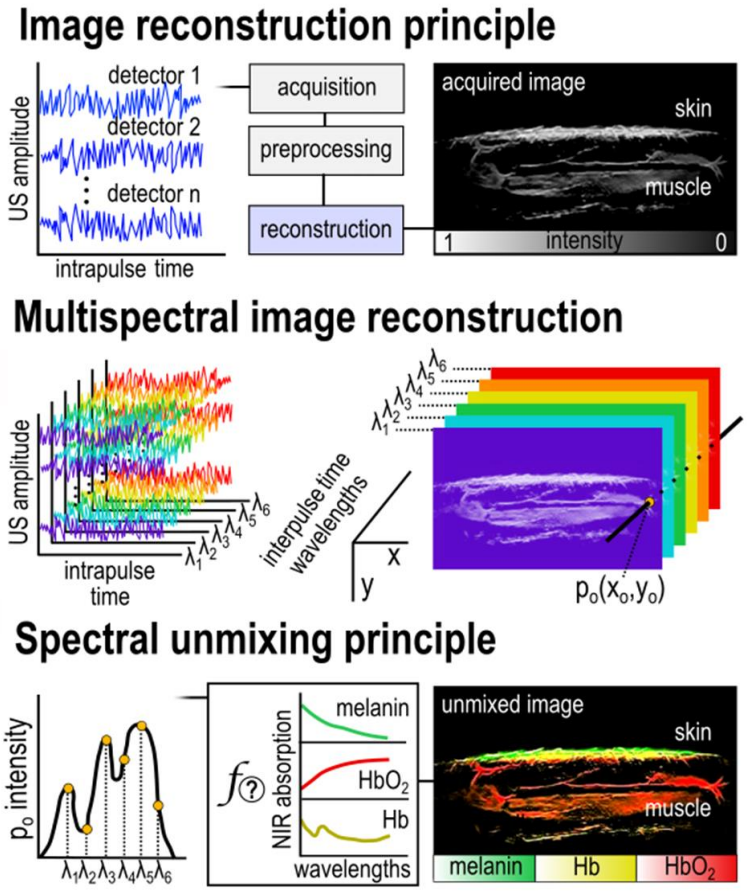

Fig. 1.4. MSOT data processing pipeline: From data acquisition to reconstruction and spectral unmixing. The signals recorded by the series of ultrasonic sensors are filtered (preprocessed) and reconstructed into planar images. For each light pulse (or else illumination wavelength), multiple (e.g. n = 256) signals are recorded and reconstructed into one image frame. As a next step, for the group of light wavelengths used for a specific scan (e.g. $\lambda_1 - \lambda_6$) a group of images are collected (multispectral stack). Finally, each pixel of the recorded multispectral stack is unmixed for a set of chromophores (e.g. melanin, oxygenated and deoxygenated hemoglobin) and the images are 'colorized' without the need for injected contrast agents. Adapted with permission from [17].

1.6 Endogenous sources of optoacoustic contrast

Apart from the numerous exogenous optoacoustic contrast agents already introduced for preclinical applications or even approved for clinical use (e.g. ICG, gold nanoparticles), it is the strong presence of endogenous chromophores in living tissue which allows for the non-invasive and label-free anatomic, functional and molecular imaging using MSOT [17]. The main endogenous absorbers in human tissues are the hemoglobins (both HbO_2 and Hb), the lipids and the water. A unique spectral signature at the NIR characterizes each light absorbing molecule (Fig. 1.5). This spectral signature has been measured and validated in the laboratory setting in previous experimental studies and is used to perform the spectral unmixing of each pixel of the recorded MSOT images, as described in previous section (Section 1.5).

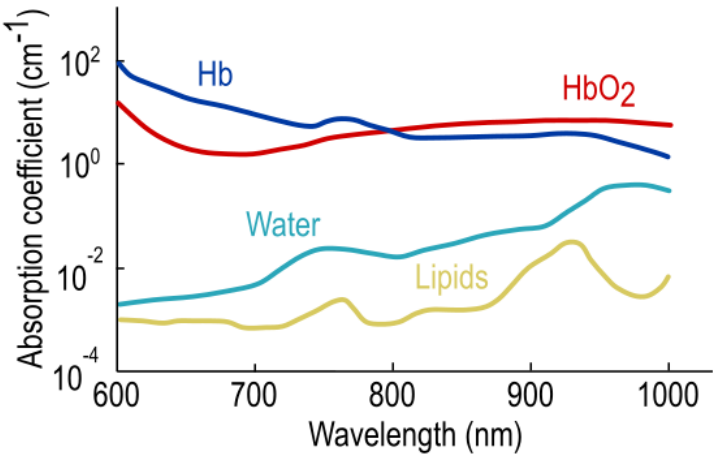

Fig. 1.5. The main endogenous light absorbers detected with MSOT and their absorption spectra in the NIR. The most prominent light absorbers at this range are the hemoglobins (HbO_2 and Hb), even if water and lipids demonstrate a peak absorption around 970 nm and 930 nm correspondingly. Nevertheless, the different morphology of the measured spectra allows for their identification and unmixing of the various absorbers during the spectral unmixing step.

Each recorded MSOT image, even if it represents a single illumination wavelength, may include partially 'specific' information for a discrete absorber. For example, at 750 nm Hb absorbs significantly more than then HbO_2 and all other main endogenous chromophores (e.g.

lipids, water etc.). Thus, MSOT images at the 750 nm are considered to mainly visualize the distribution of deoxygenated hemoglobin even if all the other endogenous absorbers absorb light as well at this wavelength. Similarly, images acquired at the 850 nm are considered to be characteristic for the oxygenated hemoglobin, images at the 930 nm for the lipids and images recorded at the 970 nm for the tissue water content. The 800 nm correspond to the 'isosbestic' point of hemoglobin where the absorptions of the oxy- and the deoxy-hemoglobin are equal. Therefore, this wavelength is considered to represent the distribution of the total hemoglobin (THb) or blood within the examined tissue.

1.7 Vascular imaging

The vascular system is a complex network of pipes and cavities aiming at delivering nutrients to tissues to meet metabolic demands. Vascular disease, such as atherosclerosis, thrombosis, trauma and inflammation compromise the structural and functional integrity of the vascular system and indirectly the metabolism of the target tissue. Vascular imaging consists a crucial tool for the diagnosis of vascular disease or the assessment of an applied therapy, either pharmacological or operative. Nowadays, several techniques enable vascular imaging in the clinic.

Ultrasound imaging provides both structural (lumen size and wall thickness) and functional (blood flow velocity and direction) information with a spatial resolution of almost 0.5mm in real time. Contrast-enhanced ultrasound (CEUS) further enhances the intraluminal contrast of conventional ultrasonography via the usually intravenous injection of microbubbles [34] . Such as technique, even if the microbubbles remain in the vascular bed for no more than 3 min, may offer invaluable information for answering targeted questions of the clinical practice, such as the complete or partial occlusion of the internal carotid artery, the presence of endoleak within the sack of a stented abdominal aneurysm or even the microvascular perfusion of a carotid plaque.

Contrast-enhanced X-ray angiography, computed tomography (CTA) and magnetic resonance imaging (MRA) provide comprehensive visualizations of the vascular lumen and its stenoses due to atherosclerosis or thrombosis without information about the vascular wall itself or the perfused target tissue. Moreover, positron emission tomography (PET) gives molecular information about active inflammation of the vascular wall, such as in the cases of atherosclerotic plaque inflammation [35], vasculitis or stent infections.

Nevertheless, even if reach in diagnostic information about the vascular pathologies described above, no direct information about the perfusion and metabolism of the target tissue is provided by any of the above-mentioned modalities. In other words, no information about the target organ of the vascular pathology or else the source of the clinical symptoms to be treated is provided. Furthermore, these technologies provide only complementary information rendering the subsequent use of several imaging modalities (e.g. ultrasound, angiography and PET) necessary for acquiring complete visualizations of disease-induced changes at a structural, functional and molecular level. Thus, the development of imaging technologies for the direct visualization of tissue metabolic changes in vascular disease and ideally the development of techniques which provide structural, functional and molecular visualizations of the vascular system along with metabolic imaging of the perfused target tissue is necessary more than ever before.

1.8 Vasometabolic coupling theory

Tissue functional status is defined by the degree of coupling between metabolic demand and vascular supply achieved locally (Fig. 1.6). On the one hand, increased metabolic demand (e.g. in exercising muscle) is followed by local vasodilation, increased vascular recruitment and thus, increased blood perfusion. On the other hand, low metabolic activity (e.g. in muscle at rest) does not require any vasodilation, vascular recruitment or extra blood perfusion to meet demands. This strong vasometabolic coupling is today the basis of several functional imaging

applications in translational medicine and everyday clinical practice, such as cancer diagnostics, brain and cardiovascular imaging.

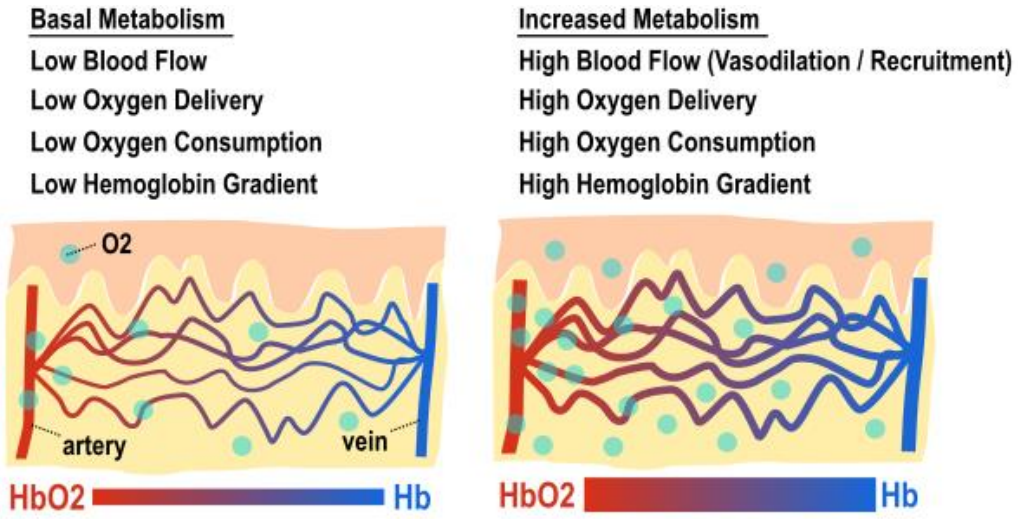

Fig. 1.6. The vasometabolic coupling theory. An increase in metabolic demands (e.g. during tissue activation, hyperactive tumors etc.) leads to the release of vasodilatatory molecules, which increase tissue perfusion and delivery of oxygen and nutrients in order to help meeting increased metabolic demands.

1.9 Metabolic or vasometabolic imaging

Tissue metabolic rate and level of function are closely related to the local regulation of blood flow and nutrients (e.g. oxygen) or contrast agents transport. This is the basis of a wide range of modern clinical imaging techniques, summarized under the term "metabolic" or "vasometabolic" imaging. Functional magnetic resonance imaging (fMRI) [36], nuclear medicine techniques (e.g. positron emission tomography, PET) and contrast-enhanced ultrasound (CEUS) are the main representatives of vasometabolic imaging in the clinics. fMRI is mainly used for brain imaging applications, such as the surgical planning for tumor resection surgery, epilepsy diagnostics or brain trauma [36-38]. Basis of fMRI is the coupling between neuronal brain activity and cerebral perfusion: a localized increase of neuronal activity is followed by increased blood flow and oxygen consumption to metabolize glucose, the main source of energy for neurons. As oxygen is being consumed, its carrier, the oxyhemoglobin

turns into deoxyhemoglobin, a magnetic molecule which produces the detected fMRI signal. fMRI offers a spatial resolution of ~1-2 mm and a temporal resolution of ~1 sec [36]. Of approximately the same spatial and temporal resolution is PET. PET is used for brain imaging, tumor imaging (e.g. lymphomas, lung cancer), myocardial flow imaging, imaging of inflammation and muscle imaging [39-41]. PET requires the injection of a specific radioactive tracer bound with a biologically active molecule (e.g. fludeoxyglucose, FDG) depending on application. PET is based on the radically increased blood flow and uptake of the biologically active molecule within the metabolically active tissue, compared to neighboring tissues. CEUS is based on the injection of either untargeted microbubbles to visualize tissue blood perfusion (e.g. brown fat tissue, skeletal muscle, liver tumors) or targeted microbubbles that bind molecules specific for a process, such as inflammation, thrombosis or angiogenesis [42-44]. CEUS provides real time imaging (at framerates of ~50 Hz) with excellent spatial resolution of ~50-100 μm.

Infrared imaging techniques, such as optical, optoacoustic and thermal, employ infrared radiation to visualize large and small blood vessels, tissue blood perfusion and metabolism providing reach information on tissue functional status. Infrared imaging techniques do not necessarily require the administration of contrast agent techniques, do not employ ionizing radiation while being low cost solutions compared to the abovementioned techniques. Most in vivo infrared techniques operate at the near-infrared (NIR, ~700-1100nm), the short wavelength infrared (SWIR, ~1100-3000nm) and the far infrared (FIR, ~ 5000-14000 nm) bands. On the one hand, NI and SWI radiation has the form of light and reaches higher depths within living tissue compared to light of other wavelengths (e.g. visible, ~400-700 nm), taking advantage of the infrared optical windows (first 650-950 nm and 1000-1350 nm) where tissue scatters and absorbs light to a much lower extent. On the other hand, at the FIR band, only heat can be visualized providing information on thermal changes driven by metabolic and hemodynamic changes following tissue activation.

Recently, optoacoustic imaging has been suggested for vascular and vasometabolic imaging. Optoacoustics, even if with limitations (see Section 1.11) provides the unique opportunity to image vasculature, perfusion and oxygen metabolism based solely on the presence of hemoglobin in tissues. Thus, optoacoustics may serve as a powerful tool which uses direct imaging of blood perfusion and oxygen metabolism at different scales (macrovascular, microvascular and tissue) to deduce information about tissue activity, function and metabolism.

1.10 Vasometabolic imaging using optoacoustics

The capability to visualize hemoglobin in blood vessels and soft tissue renders optoacoustics an ideal tool to image tissue function and metabolism based on the vasometabolic coupling theory. This way, valuable interactions between structure and function or among different biological processes could be further investigated or revealed. Several optoacoustic technologies, described in more detail before (e.g. OAM, RSOM and MSOT), could be employed for imaging based on the vasometabolic principle taking into account that optoacoustic imaging offers an extraordinary option with strong translational potential: to pass from solely vascular and metabolic to vasometabolic approaches for imaging the vasculature physiology and pathology (e.g. atherosclerosis) as well as the metabolic status of the affected organ.

An appropriate example to demonstrate the capability of MSOT to perform translational vasometabolic imaging is the imaging of brow adipose tissue (BAT) activation in mice and humans [32, 45]. In this study, we were able to demonstrate the capability of MSOT of: 1. Detecting BAT activation in both mice and humans without the need for injected contrast agents and 2. Differentiating the BAT from other soft tissues, such the white fat tissue (WAT) and the skeletal muscle based only on the MSOT-recorded absorption spectra for these tissues. BAT in mice was activated via the intravenous injection of noradrenaline, while BAT in humans was activated via cold exposure.

Fig. 1.7 depicts an example of BAT imaging with MSOT in humans. It is clear that MSOT can image the supraclavicular BAT region (Fig. 1.7a and 1.7c), as validated via the corresponding ultrasound image (Fig. 1.7.b), and further differentiate between BAT and WAT based only on the recorded spectral information within the corresponding anatomic areas (Fig. 1.7.d). Finally, MSOT was able to detect the activation of supraclavicular BAT in patients with previously detected BAT (with PET) after cold water activation by directly visualizing the strong vasodilation within the BAT region at 800 nm: the isosbestic point of HbO_2 and Hb, or else the frame showing the spatial distribution of total hemoglobin in the imaged tissue.

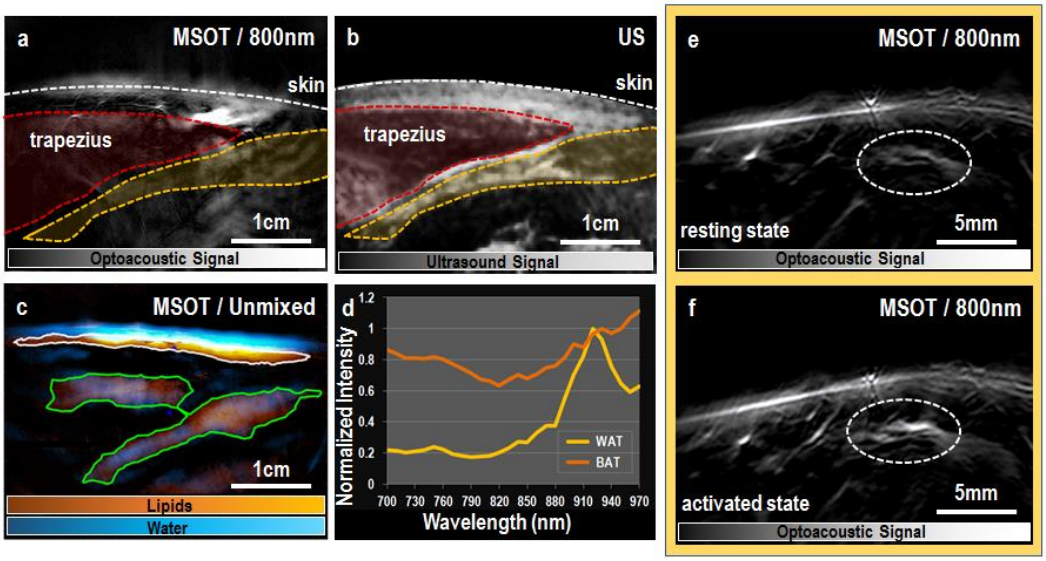

Figure 1.7. MSOT imaging of BAT and WAT. (a). MSOT image at 800 nm (isosbestic point of hemoglobins) over the supraclavicular region of a healthy volunteer. (b). Corresponding traditional ultrasound frame of the same anatomic region as in (a). (c) Unmixed MSOT image depicting the distributions of lipids and water in one frame (overlaid) over the same anatomic region. (d) Normalized spectra of the pixels belonging to the white fat (WAT, subcutaneous white region in (c)) and brown fat (BAT, yellow region in (a) and (b) and right green region in (c)) regions. (e) MSOT image at 800 nm over the supraclavicular region of a patient with previously detected BAT with BAT at resting state (before activation). (f) Same MSOT image at 800 nm as in (e) after BAT activation via cold exposure. The dotted circle depicts a dilated and perfused blood vessel. Reprinted with permission from [45].

Further examples of vasometabolic imaging using MSOT may include the imaging of inflammation, muscle activation during exercise, benign or malignant tumors etc. So far,

MSOT has been used for imaging the chronic intestinal inflammation in Crohn's disease [46], muscle perfusion and oxygenation after bicycle exercise [47] and the characterization of breast cancer tumors [16]. Abovementioned applications demonstrate the great potential of optoacoustic imaging techniques for vasometabolic imaging applications.

1.11 Limitations of optoacoustic imaging

Even if demonstrating great potential for preclinical research and clinical applications, optoacoustic imaging does not come without limitations. Current systems (clinical or preclinical) offer limited field of view of the scanned region. The produced ultrasound signals absorbed light absorption in tissue travel towards all possible directions in three-dimensional space. Thus, an ideal spherical detector would be able to collect all produced signals by a specific light-absorbing object or source and provide all the required input to the reconstruction algorithm employed. Nevertheless, due to practical reasons, more flexible and user-friendly detector arrays are used in everyday practice, limiting however the information recorded and degrading the accuracy and quality of the images reconstructed.

As mentioned above (please see Section 1.5), illumination at many different wavelengths to achieve high spectral quality and increase the accuracy of the spectral unmixing step, prolongs the duration of each multispectral stack, rendering the final outcome vulnerable to motion artifacts. The per-pixel spectral unmixing process, in particular, is prone to artifacts arising from both exogenous and endogenous motion. For example, random patient movements, fast hand movements of the MSOT operator, breathing motion and heart or vascular pulsation motion may cause prominent spectral unmixing errors. To this end, the definition of specific MSOT scanning methodologies for each anatomical region or application and the development of motion correction schemes are needed.

Furthermore, current spectral unmixing approaches are based on the known spectra, as measured in the laboratory, of specific chromophores to assign a chromophore label to each pixel of the unmixed MSOT image. Nevertheless, the strong and varying light-tissue

interaction phenomena (e.g. scattering and absorption) distort the apparent laboratory-measured spectrum travelling through different tissues with increasing depth. This phenomenon, which is known as 'spectral coloring' may further complicate the spectral unmixing process at increasing depths by introducing calculation errors. Several advanced techniques have been introduced and tested in animal models to address the abovementioned issue [48].

Even if the acquisition of optoacoustic data is real-time, further data processing (e.g. reconstruction with an advanced method, spectral unmixing) and analysis may be time-consuming. Furthermore, the volume of the recorded data may be high rendering its management a challenging issue.

Finally, as discussed, optoacoustic imaging systems can reach depths of ≈2-4 cm depending on tissue type. These penetration depths are considered unprecedented compared to purely optical techniques, but poor compared to other tomographic imaging techniques employed in the clinical setting (e.g. CT, MRI, US). However, even if this feature narrows down the range of possible applications, there is still place for numerous research and clinical questions to be answered by means of optoacoustic imaging.

1.12 Conclusions and further directions

To sum up, the current study presents several comprehensive examples underlying the unique potential of optoacoustic imaging: to provide simultaneous imaging of both the vasculature and the perfused tissue under normal or disease conditions with important implications for translational research and future clinical diagnostics of vascular and metabolic disease (e.g. diabetes mellitus, obesity etc.).

As a first step (Chapter 1), we provided a comprehensive introduction of translational optical and optoacoustic imaging, a thorough description of the optoacoustic effect and available optoacoustic technologies as well as the steps followed to achieve non-invasive and label-free vasometabolic imaging. Next, we discussed the capability of MSOT to visualize BAT activity

based on hemoglobin gradients and differentiate it from WAT, based purely on spectral characteristics of the examined tissue.

In the following chapter (Chapter 2), we explore the option to image the human peripheral macrovasculature and conduct functional challenges with clinical relevance, such as the flow-mediated dilatation (FMD) test: a great tool for diagnosing arterial endothelial dysfunction, an early step of atherosclerosis and a predictor of cardiovascular disease. In this work, vascular MSOT readouts were validated via the use of traditional vascular ultrasound.

Going one step further (Chapter 3), we examine the possibility of employing optoacoustic microscopy to analyse atherosclerotic tissue excised from human carotid arteries, a leading cause of morbidity and mortality worldwide. In this work, biological samples were scanned by means of a hybrid microscope revealing interesting interactions among different microscopic modalities.

Thus, our work showcases the great capability of optoacoustic imaging for:

- multiscale arterial imaging and atherosclerosis from macroscopy to microscopy,
- functional imaging of arterial wall dynamics in real-time,
- visualizing changes in oxygen metabolism in soft tissues based on both raw and unmixed data,

rendering optoacoustics an ideal tool for preclinical and clinical vasometabolic applications. A logical next step would be the conduction large-scale preclinical and clinical studies to investigate the precision and reproducibility of such measurements. Vascular studies to detect and quantify arterial and venous disease as well as metabolic studies on the target organs such as the skeletal muscle would serve this goal. Furthermore, we aim at expanding our studies in the fields of metabolic diseases, such as diabetes mellitus, obesity, fatty liver disease etc.

The great variability of applications requires a wide variability of tailored system designs for effective tissue illumination and ultrasound sensing. Novel systems with switchable central frequency or illumination energy, as well as, wearable optoacoustic sensors or robot-assisted

configurations would further widen the range of applications and facilitate the data acquisition process under different settings (e.g. during muscle exercise).

As already discussed, the large volume of optoacoustic data requires long data analysis times. Further advances in software development as well as artificial intelligence (AI) approaches would enable the conduction of large-scale and longitudinal preclinical and clinical studies. AI may also be used to reveal hidden correlations between optoacoustic technologies and other clinically established imaging modalities to further enhance its role as technique complementary to the existing ones used for clinical diagnostics. Moreover, the design and application of quality control mechanisms is expected to enable the conduction of randomized clinical studies and further boost the translation of optoacoustic imaging technologies in the clinics.

1.13 References

1. V. Ntziachristos, "Clinical translation of optical and optoacoustic imaging," research-article 2011-11-28 2011, doi: doi:10.1098/rsta.2011.0270.

2. K. E. Tipirneni et al., "Fluorescence Imaging for Cancer Screening and Surveillance," (in eng), Molecular imaging and biology: MIB: the official publication of the Academy of Molecular Imaging, vol. 19, no. 5, pp. 645-655, Oct 2017, doi: 10.1007/s11307-017-1050-5.

3. S. Gao et al., "Near-infrared fluorescence imaging of cancer cells and tumors through specific biosynthesis of silver nanoclusters," (in En), Scientific reports, OriginalPaper vol. 4, no. 1, pp. 1-6, 2014-03-17 2014, doi:10.1038/srep04384.

4. C. Detter et al., "Fluorescent cardiac imaging: a novel intraoperative method for quantitative assessment of myocardial perfusion during graded coronary artery stenosis," (in eng), Circulation, vol. 116, no. 9, pp. 1007-14, Aug 28 2007, doi: 10.1161/circulationaha.106.655936.

5. D. Bozhko et al., "Quantitative intravascular biological fluorescence-ultrasound imaging of coronary and peripheral arteries in vivo," (in eng), European heart journal cardiovascular Imaging, vol. 18, no. 11, pp. 1253 1261, Dec 27 2016, doi: 10.1093/ehjci/jew222.

6. T. Sanchez et al., "Metabolic imaging with the use of fluorescence lifetime imaging microscopy (FLIM) accurately detects mitochondrial dysfunction in mouse oocytes," (in eng), Fertil Steril, vol. 110, no. 7, pp. 1387 1397, Dec 2018, doi: 10.1016/j.fertnstert.2018.07.022.

7. H. Wang et al., "A dual Ucp1 reporter mouse model for imaging and quantitation of brown and brite fat recruitment," Molecular Metabolism, vol. 20, pp. 14-27, 2019/02/01/ 2019, doi: 10.1016/j.molmet.2018.11.009.

8. J. Zhao et al., "Recent developments in multimodality fluorescence imaging probes," in Acta Pharm Sin B, vol. 8, no. 3), 2018, pp. 320-38.

9. M. Chen, M. Miki, S. Lin, and S. Yung Choi, "Sodium Fluorescein Staining of the Cornea for the Diagnosis of Dry Eye: A Comparison of Three Eye Solutions," in Med Hypothesis Discov Innov Ophthalmol, vol. 6, no. 4), 2017, pp. 105-9.

10. H. C. Riess et al., "Initial experience with a new quantitative assessment tool for fluorescent imaging in peripheral artery disease," (in eng), Vasa, vol. 46, no. 5, pp. 383-388, Aug 2017, doi: 10.1024/0301 1526/a000642.

11. B. Kogon et al., "The role of intraoperative indocyanine green fluorescence angiography in pediatric cardiac surgery," (in eng), Ann Thorac Surg, vol. 88, no. 2, pp. 632-6, Aug 2009, doi: 10.1016/j.athoracsur.2009.03.010.

12. A. Ale, V. Ermolayev, E. Herzog, C. Cohrs, M. H. de Angelis, and V. Ntziachristos, "FMT-XCT: in vivo animal studies with hybrid fluorescence molecular tomography-X-ray computed tomography," (in eng), Nat Methods, vol. 9, no. 6, pp. 615-20, Jun 2012, doi: 10.1038/nmeth.2014.

13. M. D. Wheelock, J. P. Culver, and A. T. Eggebrecht, "High-density diffuse optical tomography for imaging human brain function," in Rev Sci Instrum, vol. 90, no. 5), 2019.

14. M. A. Khalil et al., "Detection of Peripheral Arterial Disease Within the Foot Using Vascular Optical Tomographic Imaging: A Clinical Pilot Study," (in eng), European journal of vascular and endovascular surgery: the official journal of the European Society for Vascular Surgery, vol. 49, no. 1, pp. 83-9, Jan 2015, doi: 10.1016/j.ejvs.2014.10.010.

15. A. Taruttis and V. Ntziachristos, "Advances in real-time multispectral optoacoustic imaging and ist applications," Nat Photonics, vol. 9, pp. 219-227, 2015, doi: 10.1038/nphoton.2015.29.

16. G. Diot et al., "Multispectral Optoacoustic Tomography (MSOT) of Human Breast Cancer," (in eng), Clinical cancer research : an official journal of the American Association for Cancer Research, vol. 23, no. 22, pp. 6912-6922, Nov 15 2017, doi: 10.1158/1078-0432.ccr-16-3200.

17. A. Karlas et al., "Cardiovascular optoacoustics: From mice to men - A review," (in eng), Photoacoustics, vol. 14, pp. 19-30, Jun 2019, doi: 10.1016/j.pacs.2019.03.001.

18. V. Ntziachristos, M. A. Pleitez, S. Aime, and K. M. Brindle, "Emerging Technologies to Image Tissue Metabolism," (in eng), Cell Metab, vol. 29, no. 3, pp. 518-538, Mar 5 2019, doi: 10.1016/j.cmet.2018.09.004.

19. C. Lutzweiler and D. Razansky, "Optoacoustic imaging and tomography: reconstruction approaches and outstanding challenges in image performance and quantification.," (in en), Sensors (Basel), vol. 13, pp. 7345-84, 2013, doi: 10.3390/s130607345.

20. A. Taruttis, G. M. van Dam, and V. Ntziachristos, "Mesoscopic and Macroscopic Optoacoustic Imaging of Cancer," Cancer Research, vol. 75, no. 8, pp. 1548-59, 2015.

21. T. Jin, H. Guo, H. Jiang, B. Ke, and L. Xi, "Portable optical resolution photoacoustic microscopy (pORPAM) for human oral imaging," (in eng), Opt Lett, vol. 42, no. 21, pp. 4434-4437, Nov 1 2017, doi: 10.1364/ol.42.004434.

22. B. Ning et al., "Ultrasound-aided Multi-parametric Photoacoustic Microscopy of the Mouse Brain," (in En), Scientific reports, OriginalPaper vol. 5, no. 1, pp. 1-7, 2015-12-21 2015, doi: doi:10.1038/srep18775.

23. C. Zhang, Y.-J. Cheng, J. Chen, S. Wickline, and L. V. Wang, "Label-free photoacoustic microscopy of myocardial sheet architecture.," Journal of biomedical optics, vol. 17, p. 060506, 2012, doi: 10.1117/1.JBO.17.6.060506.

24. M. Seeger, A. Karlas, D. Soliman, J. Pelisek, and V. Ntziachristos, "Multimodal optoacoustic and multiphoton microscopy of human carotid atheroma," (in eng), Photoacoustics, vol. 4, no. 3, pp. 102-11, 2016, doi: 10.1016/j.pacs.2016.07.001.

25. M. Schwarz, M. Omar, A. Buehler, J. Aguirre, and V. Ntziachristos, "Implications of ultrasound frequency in optoacoustic mesoscopy of the skin," (in eng), IEEE transactions on medical imaging, vol. 34, no. 2, pp. 672 7, Feb 2015, doi: 10.1109/tmi.2014.2365239.

26. J. Aguirre et al., "Precision assessment of label-free psoriasis biomarkers with ultra-broadband optoacoustic mesoscopy," Nat Biomed Eng, Article vol. 1, p. 0068, 05/10/online 2017. [Online]. Available: http://dx.doi.org/10.1038/s41551-017-0068.

27. M. Wu, K. Jansen, G. Springeling, A. F. van der Steen, and G. van Soest, "Impact of device geometry on the imaging characteristics of an intravascular photoacoustic catheter," (in eng), Applied optics, vol. 53, no. 34, pp. 8131-9, Dec 01 2014, doi: 10.1364/ao.53.008131.

28. D. VanderLaan, A. B. Karpiouk, D. Yeager, and S. Emelianov, "Real-Time Intravascular Ultrasound and Photoacoustic Imaging," (in eng), IEEE Trans Ultrason Ferroelectr Freq Control, vol. 64, no. 1, pp. 141-149, Jan 2017, doi: 10.1109/tuffc.2016.2640952.

29. Kruizinga et al., "Photoacoustic imaging of carotid artery atherosclerosis," Journal of biomedical optics, vol. 19, no. 11, pp. 110504-110504, 2014, doi: 10.1117/1.JBO.19.11.110504.

30. J. Pelisek et al., "Biobanking: Objectives, Requirements, and Future Challenges-Experiences from the Munich Vascular Biobank," (in eng), Journal of clinical medicine, vol. 8, no. 2, Feb 16 2019, doi: 10.3390/jcm8020251.

31. V. Ntziachristos and D. Razansky, "Molecular imaging by means of multispectral optoacoustic tomography (MSOT)." Chemical reviews, vol. 110, pp. 2783-94, 2010, doi: 10.1021/cr9002566.

32. J. Reber et al., "Non-invasive Measurement of Brown Fat Metabolism Based on Optoacoustic Imaging of Hemoglobin Gradients," Cell Metabolism, vol. 27, no. 3, pp. 689-701.e4, 2018, doi: 10.1016/j.cmet.2018.02.002.

33. A. Taruttis and V. Ntziachristos, "Advances in real-time multispectral optoacoustic imaging and ist applications," Nat Photon, Review vol. 9, no. 4, pp. 219-227, 04//print 2015, doi: 10.1038/nphoton.2015.29.

34. K. S. Mehta, J. J. Lee, A. A. Taha, E. Avgerinos, and R. A. Chaer, "Vascular applications of contrast enhanced ultrasound imaging," (in eng), Journal of vascular surgery, vol. 66, no. 1, pp. 266-274, Jul 2017, doi: 10.1016/j.jvs.2016.12.133.

35. K. Toutouzas et al., "Inflamed human carotid plaques evaluated by PET/CT exhibit increased temperature: insights from an in vivo study," (in eng), European heart journal cardiovascular Imaging, vol. 18, no. 11, pp. 1236-1244, Nov 1 2017, doi: 10.1093/ehjci/jew219.

36. G. H. Glover, "Overview of Functional Magnetic Resonance Imaging," (in eng), Neurosurg Clin N Am, vol. 22, no. 2, pp. 133-9, Apr 2011, doi: 10.1016/j.nec.2010.11.001.

37. C. Kesavadas and B. Thomas, "Clinical applications of functional MRI in epilepsy," in Indian J Radiol Imaging, vol. 18, no. 3), 2008, pp. 210-7.

38. J. D. Medaglia, "Functional Neuroimaging in Traumatic Brain Injury: From Nodes to Networks," (in eng), Front Neurol, vol. 8, 2017, doi: 10.3389/fneur.2017.00407.

39. A. Almuhaideb, N. Papathanasiou, and J. Bomanji, "18F-FDG PET/CT Imaging In Oncology," in Ann Saudi Med, vol. 31, no. 1), 2011, pp. 3-13.

40. R. S. Driessen, P. G. Raijmakers, W. J. Stuijfzand, and P. Knaapen, "Myocardial perfusion imaging with PET," in Int J Cardiovasc Imaging, vol. 33, no. 7), 2017, pp. 1021-31.

41. G. K. Parida, S. G. Roy, and R. Kumar, "FDG-PET/CT in Skeletal Muscle: Pitfalls and Pathologies," (in eng), Semin Nucl Med, vol. 47, no. 4, pp. 362-372, Jul 2017, doi: 10.1053/j.semnuclmed.2017.02.003.

42. A. Flynn et al., "Contrast-Enhanced Ultrasound: A Novel Noninvasive, Nonionizing Method for the Detection of Brown Adipose Tissue in Humans," (in eng), J Am Soc Echocardiogr, vol. 28, no. 10, pp. 1247-54, Oct 2015, doi: 10.1016/j.echo.2015.06.014.

43. M. Krix et al., "Assessment of skeletal muscle perfusion using contrast-enhanced ultrasonography," (in eng), Journal of ultrasound in medicine : official journal of the American Institute of Ultrasound in Medicine, vol. 24, no. 4, pp. 431-41, Apr 2005. [Online]. Available: http://dx.doi.org/.

44. J. G. Zarzour, K. K. Porter, H. Tchelepi, and M. L. Robbin, "Contrast-enhanced ultrasound of benign liver lesions," (in eng), Abdom Radiol (NY), vol. 43, no. 4, pp. 848-860, Apr 2018, doi: 10.1007/s00261-017-1402-2.

45. A. Karlas, J. Reber, E. Liapis, K. Paul-Yuan, and V. Ntziachristos, "Multispectral Optoacoustic Tomography of Brown Adipose Tissue," (in eng), Handb Exp Pharmacol, vol. 251, pp. 325-336, 2019, doi: 10.1007/164_2018_141.

46. F. Knieling et al., "Multispectral Optoacoustic Tomography for Assessment of Crohn's Disease Activity," (in eng), N Engl J Med, vol. 376, no. 13, pp. 1292-1294, Mar 30 2017, doi: 10.1056/NEJMc1612455.

47. G. Diot, A. Dima, and V. Ntziachristos, "Multispectral opto-acoustic tomography of exercised muscle oxygenation.," Opt Lett, vol. 40, pp. 1496-9, 2015.

48. S. Tzoumas et al., "Eigenspectra optoacoustic tomography achieves quantitative blood oxygenation imaging deep in tissues.," Nat Commun, vol. 7, p. 12121, 2016, doi: 10.1038/ncomms12121.

2 Clinical Flow-Mediated Dilatation Test using Optoacoustic Imaging

The final version of this chapter has been published:

Karlas A, Reber J, Diot G, Bozhko D, Anastasopoulou M, Ibrahim T, Schwaiger M, Hyafil F, Ntziachristos V. Flow-mediated dilatation test using optoacoustic imaging: a proof-of-concept. Biomed Opt Express. 2017 Jun 23;8(7):3395-3403.

Contribution:

AK perceived the idea, designed the study, performed the experiments, analyzed and interpreted the data and wrote the manuscript.

2.1 Introduction

Optoacoustic contrast in the near-infrared region (650-850 nm) is attributed primarily to light absorption by oxygenated and deoxygenated hemoglobin. Since blood vessels concentrate high amounts of hemoglobin, they present excellent targets for optoacoustic imaging. Recently, the capacity of optoacoustic tomography to visualize human vasculature was compared with ultrasound and Doppler ultrasound [1]. It was shown that the optoacoustic method outperforms ultrasonography, by providing a more accurate vessel representation, regarding meso- and micro-vasculature. Overall, the multispectral optoacoustic tomography (MSOT) ability to resolve human vasculature has been demonstrated in several reports, using different scanner configurations [2,3]. We have shown that image quality significantly improves when using curved ultrasound detectors, over linear detectors [4]. Moreover, recent development of fast-tuning lasers offering > 50 mJ energy per pulse has allowed the application of single-pulse-per-frame (SPPF) acquisition [5], which uses a single laser pulse to collect a cross-sectional image from tissue without averaging data from multiple pulses. SPPF minimizes motion artifacts and allows image collection at > 50 Hz frame rates. Nevertheless, the potential of SPPF for MSOT interrogation of physiological processes and vascular dynamics remains largely unexplored.

In this work we employed SPPF optoacoustic tomography using curved array detectors to characterize its utility in flow-mediated dilatation (FMD) tests. FMD, typically performed using ultrasound (US), measures the increase in the diameter of a peripheral artery in response to a temporary (usually 5 min) blood flow occlusion. These changes provide an indication of the functional status of the vascular endothelium, which is thought to influence risk of cardiovascular disease [6] and relate to atherosclerosis [7]. FMD measurements were carried out by a cardiology specialist on healthy, non-smoking Caucasian volunteers. Procedures were conducted in accordance with published guidelines on ultrasound-based endothelial-dependent FMD measurement of the brachial artery [8].

2.2 Methods

2.2.1 MSOT system and image acquisition

MSOT data were collected with a custom-built handheld system at 50 Hz frame rate [2]. A diode-pumped solid state Nd:YAG tunable laser (Spitlight DPSS OPO, Innolas Laser GmbH, Germany) was used for illumination between 700 nm and 960 nm using 8 ns pulse duration and 17 mJ energy per pulse (at 700 nm, highest-energy wavelength). Light was delivered to tissue through a fiber bundle (CeramOptec GmbH, Germany), attached next to a 256 piezoelectric elements detector with 5 MHz central frequency. The detector elements were arranged in a curved configuration with a radius of 60 mm, providing 174-degree coverage (Imasonic SAS, France). A sealed, flexible plastic membrane was placed around the detector and enclosed with water for coupling ultrasound waves from the tissue to the detector. Analog signals were sampled, amplified and recorded in parallel, using a 256-channel data acquisition card (DAQ) with 12-bit precision in each channel. High resolution (100 μm) of 60×60 mm (600×600 pixels) images were produced by a back-projection reconstruction method [9] using the ViewMSOT reconstruction software (Xvue Ltd, Greece). US data were acquired with a

commercial system (Logiq E9, GE, USA) equipped with a linear matrix array transducer (ML6-15) operating at a frequency of 12MHz.

Healthy volunteers (n=4, Subject #1: M-32, Subject #2: F-33, Subject #3: M-32, Subject #4: M-32) consumed no food, caffeine or medication for at least 10 h before the experiment, which was performed in a quiet, dark room at room temperature. They were positioned supine and the radial artery could be easily identified due to its characteristic shape and wall motion during the cardiac cycle by both US and MSOT imaging. The radial artery was imaged 5 cm proximal to the wrist joint using MSOT and 3 cm more proximally using US to avoid ultrasonic signal interference between the two hand-held probes during simultaneous imaging which significantly decreased the MSOT image quality. The artery was imaged along the transverse plane with both imaging modalities. All FMD tests were carried out according to guidelines by scanning the forearm region over the radial artery for 2 min at rest, 5 min over the cuff-based avascularization (total occlusion induced by a cuff pressure equal to the systolic blood pressure increased by 50 mmHg), and 2 min after the release of blood flow, with an MSOT frame rate of 50 Hz. MSOT data were recorded over the whole testing period and US images were acquired over 3 cardiac cycles at rest and exactly 60 sec after the release of blood flow. For the US measurements ink skin markings ensured the consistent localization of the same arterial cross-section before and 60 sec after the avascularization period.

Multiple measurements were performed over the forearm region to obtain baseline measurements and FMD readouts. At first, cross-sectional MSOT images of the forearm were obtained at different wavelengths over the (700 nm - 960 nm) spectral range clearly depicting the radial artery and several neighboring vessels due to their high hemoglobin concentration and light absorption signal. Illumination wavelength at ~800 nm was found to offer the best contrast, over other wavelengths. To increase our temporal resolution and enable the accurate tracking of the arterial wall dimensions over the whole scanning period (Fig. 2.1a), we scanned the subject #1 at a single wavelength of 800 nm. This wavelength represents the isosbestic point in the hemoglobin absorption spectrum and therefore the images are not affected by

changes in the content of oxy- and deoxygenated hemoglobin in blood vessels. The radial artery was in lateral contact with a set of parallel vessels (adjacent vessels) creating a complex vascular structure with characteristic cross-sectional shape (Fig. 2.1a, Fig. 2.1b). The precision required for this scanning session didn't allow us to simultaneously acquire US data for this volunteer due to technical reasons. For all other measurements (n=3) the MSOT recordings were multispectral (700:50:900 nm) and combined with US imaging of the radial artery at rest and exactly 60 sec after the release of blood flow to enable the comparison of the two imaging modalities (Fig. 2.4c) in terms of tracking arterial wall dimensions in humans in the clinical setting.

2.2.2 Artery segmentation and diameter tracking

To accurately determine the diameter changes of the radial artery, required by the FMD test, we performed an artery segmentation procedure, consisting of several steps. Accurate segmentation required correction of the optoacoustic signal variation across the lumen cross-section due to depth-dependent light attenuation. The vascular complex was interactively identified by the user on the first frame of the acquired image series, and this location was registered for all subsequent images acquired (Fig. 2.1a, Fig. 2.1b). All images were then converted to binary by applying a threshold based on the Otsu's global image thresholding method [10]. White pixels not connected to the vascular complex of interest were considered as noise and eliminated. The vascular complex was then fitted to an ellipse (circumscribing) and attenuation correction was applied along the short axis of the ellipse, for all areas in the original image that were above the threshold. Although photon attenuation follows an exponential decay, a linear correction sufficed herein to sufficiently smooth the signal distribution in the radial artery (Fig. 2.1c). Following attenuation correction, a second threshold was applied using Otsu's method [10] and the resulting binary silhouette of the entire radial complex was smoothed via morphological operations and the convex hull of the radial artery was finally revealed (Fig. 2.1d). To track the diameter changes of the radial artery over

time, the Fitzgibbon's direct least-squares method [11] was applied to fit an ellipse onto the edge of the binary silhouette (Fig. 2.1e). Fluctuations in the minor and major axes of the fitted ellipses were calculated over the entire FMD recording period for the subject #1 (Fig. 2.2a, Fig. 2.2b) and used to extract information about the FMD response and functional parameters of the arterial wall (e.g. wall strain, cross sectional distensibility) for every cardiac cycle. The same algorithm was applied on selected frames of the MSOT recordings before and at 60 sec after the avascularization period for all subjects to extract the FMD responses. Furthermore, the minor and major cross-sectional axes of the radial artery were measured manually by a cardiology specialist on both MSOT and US data at rest and 60 sec after the end of occlusion providing the potential to assess the performance of MSOT in comparison to the gold-standard traditional US imaging under the same conditions when imaging peripheral arteries in humans *in vivo* (Fig. 2.3a).

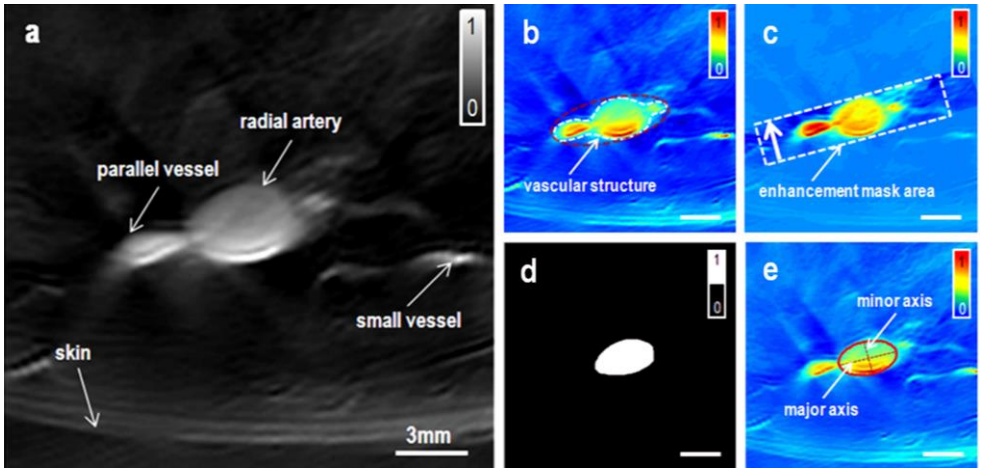

Fig. 2.1. Multispectral optoacoustic tomography (MSOT) imaging of the radial artery in the forearm region. (a) Gray-scale optoacoustic image of the radial artery and neighboring vessels obtained at 800nm prior to occlusion. (b) Same image as in (a) using a different color map with the white dashed line indicating the vascular structure of interest and the red dashed line indicating the circumscribing ellipse. (c) Result of attenuation correction step after applying the enhancement mask on the area marked with the white dashed line. The thick white arrow in the marked area indicates the direction of linear signal amplification. (d) Segmented lumen of the radial artery. (e) Final fitted ellipse with its major and minor axis representing the radial artery. All scale bars are 3mm. Reprinted with permission from [25].

2.2.3 Calculation of arterial distensibility and FMD response

By plotting the lengths of the minor axes of the fitted ellipses over the whole recording period of our first measurement (Subject #1), we observed that they follow a periodic pattern identical to the expected recording of the radial blood pressure wave over a cardiac cycle [12] (Fig. 2.2c, Fig. 2.2d). We employed the periodic pattern of the lengths of the ellipses minor axes to identify the time points corresponding to the cardiac systole and diastole. Thus, we recorded the peak of the minor axis of the ellipse as a function of time, to identify the maxima and minima for each cardiac cycle. Based on the known physiological radial blood pressure fluctuations over a cardiac cycle [12], an intuitive assumption has been made that each highest peak corresponded to the peak-systolic point in the cardiac cycle, while the next lowest peak corresponded to the end-diastolic point of the same cycle. The fluctuations in the minor axis of the ellipse during each cardiac cycle determine the per-cycle diameter-based distensibility or wall strain (WS) of the artery over the periods before and after total occlusion (Eq. 2.1 [18]):

$$WS = \frac{Ds - Dd}{Dd} \qquad \text{Eq. 2.1}$$

where Ds refers to systolic minor axis of the ellipse and Dd to diastolic minor axis. The cross-sectional distensibility (CD) was calculated based on the cross-sectional area as follows (Eq. 2.2 [18]):

$$CD = \frac{As - Ad}{Ad} \qquad \text{Eq. 2.2}$$

where As refers to systolic cross-sectional area of the ellipse and Ad to diastolic cross-sectional area. The ellipse cross-sectional area (EA) was calculated as in Eq. 2.3:

$$EA = \frac{\pi\alpha\beta}{4} \qquad \text{Eq. 2.3}$$

where α is the major axis length and β is minor axis length evaluated empirically. We then interrogated whether FMD responses can be calculated by observing the radial artery diameter,

considering the diameter as either the minor or the major axis of the fitted ellipse. FMD calculations were related to the radial artery diameter as (Eq. 2.4):

$$FMD = \frac{HD - BD}{BD} \times 100\% \qquad \text{Eq. 2.4}$$

where HD refers to the hyperemia diameter of the artery, defined as the diameter at 60 seconds after the end of occlusion, while BD refers to the baseline diameter of the measured artery at rest. The same formula was used to calculate the FMD responses for all subsequent MSOT measurements.

2.3 Results

First, we tracked the calculated minor and major axes of the radial artery over the whole MSOT recording period for the subject #1. Fig. 2.2a and Fig. 2.2b depict fluctuations in the diameter of the ellipse over 70 seconds prior to occlusion and 70 seconds after it, respectively. As expected, the lengths of both the minor and major axes of the fitted ellipse progressively decrease after the inflation of the cuff above the systolic blood pressure indicating the gradual closing of the artery. The radial artery needed about 50 seconds to close completely and become invisible on MSOT. Respectively, after the abrupt deflation of the cuff and the end of total occlusion the lengths of the two axes increase acutely indicating the acute opening of the radial artery in response to the full release of blood flow. As can be seen, changes in the minor and major axes show different temporal patterns. Fig. 2.2c and Fig. 2.2d indicate that the fluctuations of minor axis reflect more closely the physiological changes in arterial blood pressure during one cardiac cycle, enabling differentiation between the systolic and diastolic phases. In contrast, the pattern of fluctuations in major axis length, showed less variation within each cycle but greater variation across longer periods of time, as for example over the following two time periods: seconds #45-55 before occlusion (Fig. 2.2a) and seconds #10-20 seconds after occlusion (Fig. 2.2b).

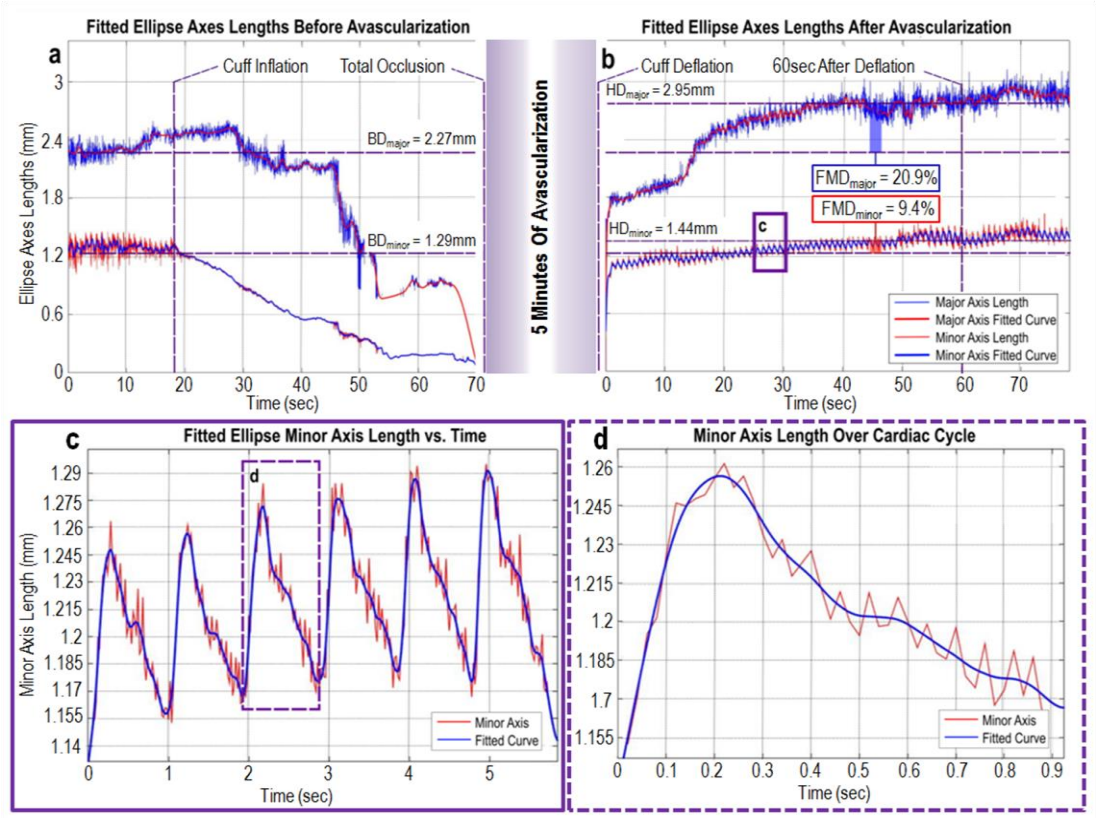

Fig. 2.2. MSOT-derived readouts of the minor and major axes of the fitted ellipse over the FMD measurement. (a) Axes fluctuations before complete arterial occlusion. (b) Axes fluctuations after a 5-min avascularization (total occlusion) period. (c) Minor axis changes over a 6-second period after release of arterial occlusion. Expanded from the boxed area in (b). (d) Fluctuations of the minor axis length during a cardiac cycle after arterial occlusion marked also in (c). Reprinted with permission from [25].

Next, we determined the per-cycle diameter-based distensibility or wall strain (WS) of the radial artery wall for subject #1, based on Eq. 2.1. We also calculated the cross-sectional distensibility (CD) based on fluctuations in best-fitting ellipse area for the same subject (Eq. 2.2, Eq. 2.3). Fig. 2.3a and Fig. 2.3b depict the beat-to-beat arterial distensibility during two 12-second periods before and after occlusion, respectively (seconds #1-12 before complete arterial occlusion occurs and seconds #54-66 after the end of complete occlusion). As can be seen, the distensibility differed before and after the end of total occlusion. It is also of interest that the distensibility at either of these time periods differed depending on whether the minor axis or ellipse area was used in the calculation.

Finally, we calculated the FMD responses for each axis for all subjects based on MSOT data. The hyperemia diameter and the baseline diameter for each axis of the fitted ellipse (HD_{minor}/HD_{major} and BD_{minor}/BD_{major}) were extracted to estimate the FMD response corresponding to each axis according to Eq. 2.4. Based on absolute minor axis measurements, the baseline diameter BD_{minor} was 1.29 mm and HD_{minor} = 1.44 mm, corresponding to FMD_{minor} of 9.4%. A much higher FMD_{major} of 20.9% was obtained using the extracted major axis values (BD_{major} = 2.27 mm, HD_{major} = 2.95 mm). Nevertheless, both FMD calculations fell within the normal range reported in various studies, which may vary by as much 20% in the case of the brachial artery [13-15]. For all other subjects, the calculations were conducted by applying the same algorithm on selected frames of the resting period and exactly 60 sec after the end of occlusion. Fig. 2.3a shows the FMD responses for the minor and major axes of the radial artery as represented by the corresponding ellipse axes. The mean ± standard deviation of the FMD_{minor} was 11.4 ± 3.3% and of the FMD_{major} was 26.1 ± 6.4%.

As a last step, a comprehensive comparison between MSOT and traditional US imaging regarding accuracy in tracking of arterial dimensions is presented. To this end, a cardiology specialist measured the minor and major axes of the radial artery cross-section at rest and at 60 seconds after the end of cuff-occlusion on characteristic selected frames of both MSOT and US recordings for 3 subjects (Subject #2-4) (Fig. 2.4a, Fig. 2.4b). The specialist measured 3 times each axis on every provided frame and the mean value was taken as the final axis length. Fig. 2.4c depicts the absolute values of the manually measured minor and major axes of the cross-section of all radial arteries as extracted from MSOT and US data at two different time points: before occlusion and 60 sec after the end of arterial occlusion. MSOT seems to provide a clinically acceptable precision when compared to the traditional US in terms of arterial diameter assessment.

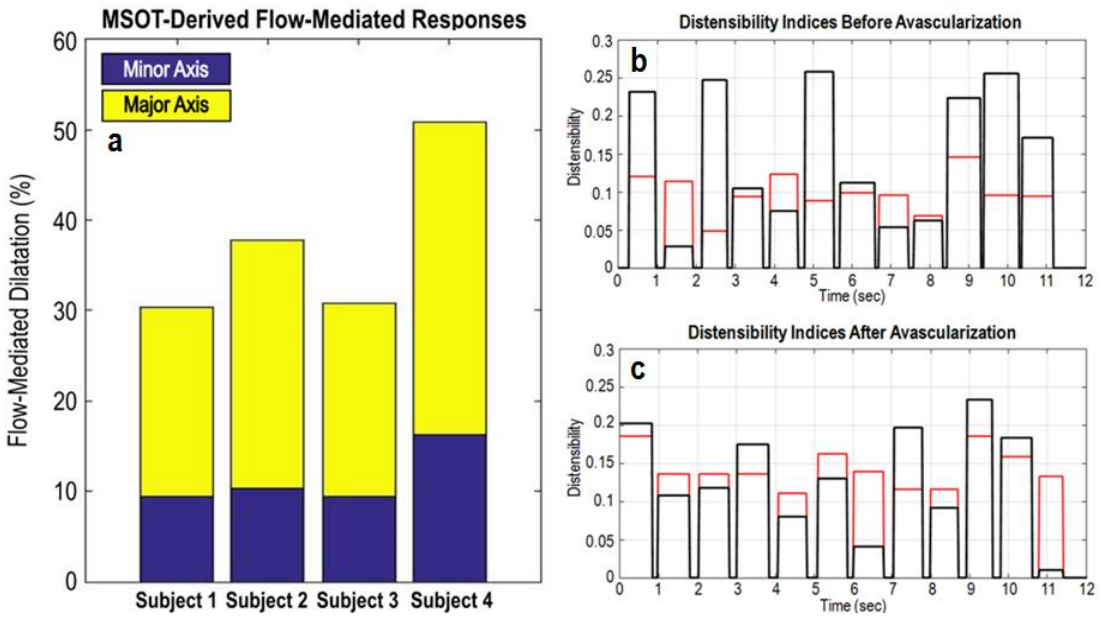

Fig. 2.3. Summarized MSOT-derived FMD results for all subjects and exemplary distensibility indices. MSOT-derived (a) MSOT-derived FMD responses for all subjects (n=4). (b,c) Calculated distensibility parameters of the radial artery. Beat-to-beat arterial distensibility before (b) and after (c) occlusion, respectively. Black bars: estimated area-based cross-sectional distensibility (CD), Red bars: diameter-based distensibility or wall strain (WS). Reprinted with permission from [25].

By using US, the minor arterial axis was calculated to be 1.97 ± 0.16 mm and the major axis 2.62 ± 0.31mm across the cohort of subjects #2, 3 and 4. By employing MSOT the minor axis was estimated to be 2.02 ± 0.22 mm and the major cross-sectional axis 2.51 ± 0.29mm. To provide a metric of the intraobserver error, as well as, the error introduced by the image quality the cardiology specialist measured both the minor and major axes of the arterial cross-section in two high-quality random MSOT and US frames at 10 different timepoints. The mean ± standard deviation values were estimated to be 1.85 ± 0.07 mm for the minor axis and 2.51 ± 0.07 mm for the major axis using US. The MSOT-derived corresponding values were: 2.47 ± 0.04 mm for the minor axis and 3.46 ± 0.05 mm for the major cross-sectional axis.

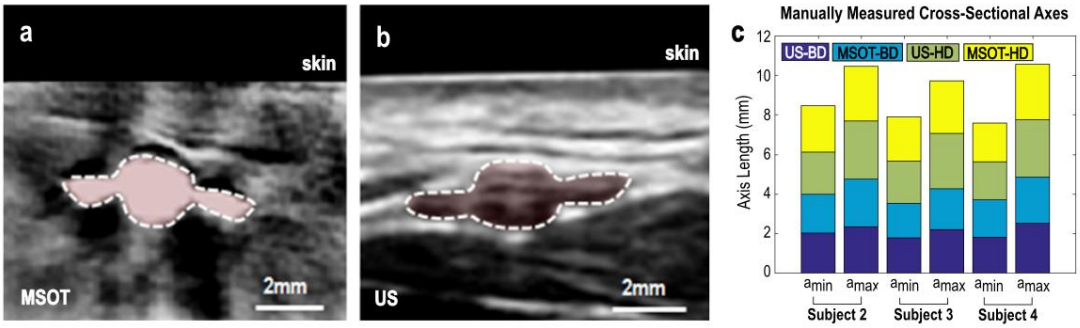

Fig. 2.4. Exemplary MSOT versus US images and summarized manually-measured cross-sectional axes. (a) Characteristic MSOT frame of the radial artery cross-section of subject #4. The dashed line delineates the vascular complex of interest. The continuous white line represents a manually defined minor axis of the radial artery cross-section, while the two white dots represent the manually defined limits of the major axis. (b) Characteristic US frame of the radial artery cross-section at rest of subject #4. Markings are the same as previously described in (a). (c) Manually measured cross-sectional arterial axes lengths for all subjects extracted from US and MSOT images before and 1 min after occlusion. BD: Baseline Diameter, HD: Hyperemia Diameter. Reprinted with permission from [25].

2.4 Discussion and conclusions

This study presents a proof of concept for the use of MSOT for real-time FMD testing of macrovascular endothelial function in humans within the clinical setting. It takes advantage of a recently developed hand-held device and a customized computational method, to image the radial artery and track changes in its diameter with high temporal resolution. MSOT FMD tests relied on imaging the radial artery cross-section and quantitatively assessing its contour using a fitted ellipse. Additional information was also obtained about arterial wall distensibility whose decrease (or else increase in wall stiffness) has been associated with raised risk of cardiovascular disease [16].

The herein described approach presents a novel and very promising tool for FMD testing which may be considered as an alternative to ultrasonography, since it offers much better vessel wall contrast and resolution compared to ultrasound images that are affected by speckle. Furthermore, MSOT demonstrates clinically acceptable accuracy compared to US with regards to the capability of tracking arterial wall dimensions (Fig. 2.4c). Ultrasound imaging usually resolves vessels along the longitudinal dimension as it offers poor vessel wall delineation in cross-sectional images [8]. Then, FMD tests are

performed by recording the arterial diameter as it is calculated based on the central longitudinal plane of the artery visualized. Compared to adjacent planes, fluctuations in the central plane of the vessel (along the longitudinal dimension) are the highest, optimizing the sensitivity in detecting vessel wall fluctuations over time. Nevertheless, accurate FMD measurements based on ultrasound imaging are challenging since they require identification of the central plane and a long-term fixation of the ultrasound probe over the long arterial axis, which can lead to errors due to motion. Conversely, transversal (cross-sectional) scanning of vessels overcome the limitations of ultrasound imaging and possibly offers greater flexibility and accuracy for precise tracking of the vessel diameters across the cross-section [17].

Nevertheless, larger cohorts and more systematic studies are needed for a detailed comparison between MSOT and US imaging not only regarding the tracking of arterial dimensions in humans *in vivo* but also the extraction of FMD readouts. A series of error sources challenges the reliability of such a comparison. At first, the artery should be imaged at the same position with both the MSOT and US probe during the same FMD recording to avoid the intrasession, intraobserver, and intrasubject variability of FMD responses [18]. The simultaneous scanning with both hand-held probes in not only technically challenging but also lowers the quality of the MSOT images due to ultrasound interference. Furthermore, the radial artery is characterized by variable diameter across its length which further influences the recorded FMD response [19]. The development of accurate automated methods for arterial segmentation in both MSOT and US images is of great importance since the manual segmentation of the arterial axes or circumference introduces a significant calculation error which further degrades the result as already discussed above. Finally, additive errors emanating from data noise, limited angle of MSOT sensor arrays, defects of the optoacoustic reconstruction methods etc. further decrease the precision of arterial size estimation, as well as, of the even more prone to error FMD readouts.

As presented, we further observed differences in the post-occlusion dilatatory responses between recordings of the minor and major cross-sectional arterial axes from subject #1. Indeed, contrary to the major axis, which showed a diphasic increase after the end of occlusion (first increase at second #0 and

second additional increase around second #15 post-occlusive; Fig. 2.1b), the response of the minor axis was monophasic and quickly stabilized at an average length, while showing fine fluctuations over the cardiac cycle. These findings show considerable axis- and plane-related variability of FMD response, which may help explain the wide range of normal FMD values in the literature [13-15]. Our findings also highlight the need for greater standardization of FMD tests and demonstrate the advantage of using a cross-sectional analysis.

Fluence correction was found necessary for improving the performance of lumen segmentation and accurate wall delineation. We observed that the mean ± standard deviation of the minor axis was 2.16 ± 0.33 mm when calculated manually, 2.11 ± 0.28 mm after applying the fluence correction and segmentation scheme, and 2.08 ± 0.22 mm after applying the ellipse fitting technique. The corresponding parameters for the major arterial axis were: 2.92 ± 0.82 mm when measured manually, 3.21 ± 0.9 mm after correcting for fluence attenuation and segmenting, and 3.18 ± 0.86 mm after applying the ellipse fitting step. The assessment of the fluence correction step took place by calculating the uniformity of energy of the gray-level co-occurrence matrix over the segmented region for each processed MSOT frame. The calculated values after applying the fluence correction mask were consistently equal or larger than the ones before correcting (e.g. from 0.263 to 0.491 for a characteristic MSOT frame of subject #1). With the proposed method we detected radial artery diameters as small as 0.17 mm (based on the minor axis; Fig. 2.2a), which is close to the resolution limit of 100 μm of the MSOT system employed. Improvements in the segmentation and tracking processes may enable monitoring of even smaller vascular structures, potentially using a fully automated framework. The herein combination of precise ellipse fitting and 50 Hz temporal resolution further allowed observation of arterial wall dynamics, which have been identified as an independent risk factor for premature cardiovascular disease [20].

Future steps of MSOT-based cardiovascular applications may make use of lipid readings for identifying atherosclerotic lesions [5, 21, 22], while the use of indocyanine green (ICG) might empower molecular studies of plaque inflammation [23]. With arrival of improved chromophores, MSOT could enable the interrogation of a wider range of processes and functions offering pathophysiological readings of

disease that may affect the FMD response [24]. The results of the current study testified the possible utility of MSOT over ultrasonography for FMD measurements. An extensive study of FMD responses on healthy volunteers and patients may lead to a precise comparison of MSOT and US and encourage future research into the assessment of arterial wall dynamics and vascular biology.

2.5 References

1. A. Taruttis, A. C. Timmermans, P. C. Wouters, M. Kacprowicz, G. M. van Dam, and V. Ntziachristos, "Optoacoustic Imaging of Human Vasculature: Feasibility by Using a Handheld Probe.," Radiology, 152160 (2016).

2. A. Dima and V. Ntziachristos, "Non-invasive carotid imaging using optoacoustic tomography.," Optics express 20, 25044-25057 (2012).

3. X. L. Deán-Ben and D. Razansky, "Functional optoacoustic human angiography with handheld video rate three dimensional scanner.," Photoacoustics 1, 68-73 (2013).

4. A. Dima, N. C. Burton, and V. Ntziachristos, "Multispectral optoacoustic tomography at 64, 128, and 256 channels," Journal of biomedical optics 19, 036021 (2014).

5. A. Taruttis and V. Ntziachristos, "Advances in real-time multispectral optoacoustic imaging and its applications," Nature Photonics 9, 219-227 (2015).

6. H. A. R. Hadi, C. S. Carr, and J. Al Suwaidi, "Endothelial dysfunction: cardiovascular risk factors, therapy, and outcome.," Vascular health and risk management 1, 183-198 (2005).

7. M. A. Gimbrone, "Vascular endothelium: an integrator of pathophysiologic stimuli in atherosclerosis.," The American journal of cardiology 75, 67B-70B (1995).

8. M. C. Corretti, T. J. Anderson, E. J. Benjamin, D. Celermajer, F. Charbonneau, M. A. Creager, J. Deanfield, H. Drexler, M. Gerhard-Herman, D. Herrington, P. Vallance, J. Vita, and R. Vogel, "Guidelines for the ultrasound assessment of endothelial-dependent flow-mediated vasodilation of the brachial artery: a report of the International Brachial Artery Reactivity Task Force.," Journal of the American College of Cardiology 39, 257-265 (2002).

9. A. Rosenthal, V. Ntziachristos, and D. Razansky, "Acoustic Inversion in Optoacoustic Tomography: A Review.," Current medical imaging reviews 9, 318-336 (2013).

10. N. Otsu, "A Threshold Selection Method from Gray-Level Histograms," IEEE Transactions on Systems, Man, and Cybernetics 9, 62-66 (1979).

11. A. Fitzgibbon, M. Pilu, and R. Fisher, "Direct least square fitting of ellipses," Pattern Analysis and Machine Intelligence, IEEE Transactions on 21, 476-480 (1999).

12. M. F. O'Rourke, A. Pauca, and X. J. Jiang, "Pulse wave analysis," Br J Clin Pharmacol 51, 507-522 (2001).

13. M. R. Adams, J. Robinson, K. E. Sorensen, J. E. Deanfield, and D. S. Celermajer, "Normal ranges for brachial artery flow-mediated dilatation: A non-invasive ultrasound test of arterial endothelial function," 2, 146-150 (1996).

14. E. Dalli, L. Segarra, J. Ruvira, E. Esteban, A. Cabrera, R. Lliso, E. López, E. Llopis, and J. F. Sotillo, "[Brachial artery flow-mediated dilation in healthy men, men with risk factors, and men with acute myocardial infarction. Importance of occlusion-cuff position]." Revista española de cardiología 55, 928-935 (2002).

15. A. Peretz, D. F. Leotta, J. H. Sullivan, C. A. Trenga, F. N. Sands, M. R. Aulet, M. Paun, E. A. Gill, and J. D. Kaufman, "Flow mediated dilation of the brachial artery: an investigation of methods requiring further standardization," BMC Cardiovascular Disorders 7, 11 (2007).

16. F. U. Mattace-Raso, T. J. van der Cammen, A. Hofman, N. M. van Popele, M. L. Bos, M. A. Schalekamp, R. Asmar, R. S. Reneman, A. P. Hoeks, M. M. Breteler, and J. C. Witteman, "Arterial stiffness and risk of coronary heart disease and stroke: the Rotterdam Study," Circulation 113, 657-663 (2006).

17. F. A. Chaudhry, S. Bangalore, S. Upadya, A. Shah, H. Eftekhari, D. Pudpud, and C. M. Sehgal, "Cross-sectional imaging identifies flow-mediated vasodilatation more accurately compared with longitudinal imaging.," Journal of the American Society of Echocardiography : official publication of the American Society of Echocardiography 20, 1380-1385 (2007).

18. M. Charakida, E. de Groot, S. P. Loukogeorgakis, T. Khan, T. Luscher, J. J. Kastelein, T. Gasser, and J. E. Deanfield, "Variability and reproducibility of flow-mediated dilatation in a multicentre clinical trial," European heart journal 34, 3501-3507 (2013).

19. A. Y. Nasr, "The radial artery and its variations: anatomical study and clinical implications," Folia morphologica 71, 252-262 (2012).

20. G. Baltgaile, "Arterial wall dynamics," Perspectives in Medicine 1, 146-151 (2012).

21. A. B. Karpiouk, B. Wang, and S. Y. Emelianov, "Development of a catheter for combined intravascular ultrasound and photoacoustic imaging.," The Review of scientific instruments 81, 014901 (2010).

22. B. Wang, A. Karpiouk, D. Yeager, J. Amirian, S. Litovsky, R. Smalling, and S. Emelianov, "In vivo intravascular ultrasound-guided photoacoustic imaging of lipid in plaques using an animal model of atherosclerosis.," Ultrasound in medicine & biology 38, 2098-2103 (2012).

23. C. Vinegoni, I. Botnaru, E. Aikawa, M. A. Calfon, Y. Iwamoto, E. J. Folco, V. Ntziachristos, R. Weissleder, P. Libby, and F. A. Jaffer, "Indocyanine green enables near-infrared fluorescence imaging of lipid-rich, inflamed atherosclerotic plaques.," Science translational medicine 3, 84ra45 (2011).

24. A. L. Huang and J. A. Vita, "Effects of systemic inflammation on endothelium-dependent vasodilation.," Trends in cardiovascular medicine 16, 15-20 (2006).

25. Karlas A, Reber J, Diot G, Bozhko D, Anastasopoulou M, Ibrahim T, Schwaiger M, Hyafil F, Ntziachristos V. Flow-mediated dilatation test using optoacoustic imaging: a proof-of-concept. Biomed Opt Express. 2017 Jun 23;8(7):3395-3403.

3 Hybrid Microscopic Optoacoustic Analysis of Human Carotid Atherosclerosis

The final version of this chapter has been published:

Seeger M*, Karlas A*, Soliman D, Pelisek J, Ntziachristos V. Multimodal optoacoustic and multiphoton microscopy of human carotid atheroma. Photoacoustics. 2016 Aug 4;4(3):102-111. *Equal contribution.

Contribution:

AK perceived the idea, designed the study, guided the experiments and the data analysis, interpreted the data and wrote the manuscript.

3.1 Introduction

Atherosclerosis, a multifactorial disease of the arterial wall, is a major precursor of ischemic heart disease and stroke; two of the leading morality causes worldwide [1]. Ischemic stroke is attributed to thrombosis and cerebral ischemia and often associated with chronic atheromatous plaque accumulating within the sub-endothelial layer (intima) of carotid arteries. Effective plaque prevention or treatment requires understanding of the mechanisms underlying atheroma formation, rupture, and consequent precipitation to acute ischemic events.

Atheroma tissue obtained from patients is a highly valuable source of information regarding the disease. It typically presents an inhomogeneous mass of high structural and biological complexity, usually consisting of lipids, inflammatory and smooth muscle cells (SMC), connective tissue, and calcium deposits [2–4]. Multiple factors (e.g. inflammatory, biomechanical, genetic, environmental) seem to be involved in all stages of atheroma formation and progression [3,4].

The discrete histopathological features of atherosclerotic plaques, reflecting different pathogenetic and pathophysiological mechanisms, allow for classification according to their severity: early, intermediate, and advanced [5]. Early lesions usually start as simple clusters of lipid-loaded macrophages before reforming to the so-called fatty streaks and giving rise to discrete lipid pools among the SMC layers along with discrete intimal thickening [6].

Intermediate lesions are the first to be described as atheromas, since they have a well-defined core of lipids usually protruding into the vascular lumen. In terms of clinical incidence, early lesions are asymptomatic while intermediate ones may already cause ischemic disturbances [7,8]. However, the presence of symptoms is usually connected to advanced (late) and complicated plaques even if the phenomenon of plaque rupture seems to be uncorrelated to parameters as plaque size and degree of luminal narrowing [7,9]. Advanced lesions are characterized by thinning of the fibrous cap and a large lipid core containing an increased amount of collagen, inflammatory cells, as well as affected SMCs. These plaques may evolve into complicated ones with superficial fissure formation, intraplaque haemorrhage (IPH), and acute luminal thrombus occurrence due to direct exposure of lipid core material to blood contents [4,5,8].

From a topographical point of view, each plaque may be roughly divided into sections corresponding to specific structural regions: the cap, the shoulders, and the core (Fig. 3.2a). According to multiple histological studies, thrombosis is usually the result of cap ulceration and rupture near to one of the shoulders [10–12]. A vulnerable plaque is generally characterized by a large necrotic core (lipids, fibrin, blood inclusions, and macrophages), a thin degraded cap (decreased collagen and SMCs), as well as prominent inflammatory and neovascularization features [13]. Plaque rupture is frequently considered to be a mechanical event. On the one hand, collagen, a basic constituent of the extracellular matrix, seems to be associated with the biomechanical integrity of the cap [14]. Its degradation and disorganization have been correlated to decreased stability of the fibrous cap [14,15], while the retrieval of collagen production (e.g. statin therapy) seems to stabilize the plaque [16]. On the other hand, red blood cells (RBC), either within the plaque's neovessels or in the form of IPH, play a crucial role in atheroma progression, destabilization, and rupture [13].

With respect to the above-mentioned histopathological evolution of atheromatous lesions linked to topographical conditions and compositions at specific regions within the plaque, new powerful and accurate imaging tools are required to precisely observe and analyse components

influencing the mechanical stability. Within this framework, the accurate identification and characterization of the histological components of an atheromatous sample could increase our knowledge of atherosclerosis and define features related to ischemic events, which would potentially serve as future therapeutic targets.

Studies of atheromas largely rely on histopathology [17–21], which can interrogate several cellular and molecular features of the disease. Conversely, histopathology is invasive and laborious, requires tissue staining and typically visualizes thin slices and small areas of the specimen. Non-invasive volumetric measurements of excised atheromas are studied by tissue-sectioning microscopy, such as confocal or multiphoton microscopy [22–25]. Nevertheless, tissue-sectioning microscopy also requires labels for cellular and sub-cellular moieties. While genetically modified animals using fluorescent reporter labels may be generated for studying atheroma events in mice, imaging of excised human specimens is problematic for use with tissue-sectioning microscopy since it requires diffusion and clearance of a label through the tissue post-mortem. Likewise, the use of fluorescence agents against specific atheroma targets have been used in animal studies [26–29] but are not readily available for human use.

The use of non-linear optical (NLO) microscopy has been suggested for label-free visualization of atheromas, based on optical harmonic detection or tissue autofluoresence. It has been shown that second harmonic generation (SHG) resolves collagen structures, two-photon excitation fluorescence (TPEF) microscopy probes nicotinamide adenine dinucleotide (NADH), elastin, and foam cells, whereby third harmonic generation (THG) microscopy can image low density lipoprotein (LDL) deposits or embedded macrophages [30–35]. Optoacoustic imaging has also been investigated for imaging atheroma and vascular moieties regarding the detection as well as distinction of lipids and hematomas [36–39]. Recently, multiphoton and optoacoustic microscopy was proposed for hybrid imaging of autofluorescence, harmonic, and absorption contrast generation [40–42], so far applied to visualize structural and cellular features in fish and small mammals.

Herein we consider the extension of label-free imaging capacities by applying multiphoton microscopy (MPM) and optoacoustic microscopy (OAM) in a pilot study to characterize atheromatous tissue. We studied whether the hybrid approach could reveal a wider feature set of investigational or clinical relevance without the need to stain the tissue. Using the intrinsically accurate registration of optical and optoacoustic microscopy images, we further researched the spatial congruence and complementarity of collagen and RBCs in human carotid atheroma, i.e. two basic components which are present in different stages of the plaque formation process and frequently altered in unstable plaques [17].

3.2 Materials and methods

3.2.1 Experimental setup

The hybrid microscopic system utilized in this study combines second and third harmonic generation (SHG and THG), two-photon excitation fluorescence (TPEF), and optical resolution optoacoustic microscopy (OAM). All modalities are characterized by a lateral resolution of about 1 µm and a maximum imaging depth of up to ~300 µm [40,41]. Hybrid multiphoton and optoacoustic microscopy (MPOM), as schematically depicted in Fig. 3.1, consists of two separate laser systems for OAM and MPM [40,41]. Both laser systems are based on a common and co-aligned beam path, which is guided consecutively into an inverted microscope (AxioObserver. D1, Zeiss, Jena, Germany). Final image generation for both systems is achieved by raster-scanning a focused optical excitation beam across the examined specimen by means of fast galvanometric mirrors (GM) (6215H, Cambridge Technology, Bedford, USA). An accurate and seamless interchange between ultrasound transducer for OAM and photomultiplier tube (PMT) for THG acquisition is accomplished by magnetic kinematic bases (SB1/M & SB1T/M, Thorlabs, New Jersey, USA), which are previously adjusted using a suture-cross reference phantom (Dafilon USP 11/0, B. Braun Melsungen AG, Melsungen, Germany). Brightfield (BF) examination of chosen regions of interest (ROI) was carried out using a CCD camera (AxioCam ICc 1, Zeiss).

3.2.2 Optoacoustic microscopy (OAM)

OAM utilizes a pulsed diode-pumped solid-state laser (Flare HP PQ Green 2k 500, Innolight GmbH, Hannover, Germany; energy per pulse: 570 µJ, pulse width: 1.8 ns, repetition rate: 1.2 kHz) as an excitation source at 515 nm. The beam is attenuated by neutral density filters and enlarged by a telescopic arrangement of lenses. In order to merge both modalities, the OAM beam is guided by a longpass dichroic mirror (DMLP650, Thorlabs) onto a high-precision set of GMs. Latter are used for raster-scanning the beam focus in the sample and are controlled by a 16-bit data acquisition card (DAQ) (PCIe 6363, National Instruments, Austin, Texas, USA; max. sampling rate per channel: 1 MS/s). Subsequently, the beam is focused by a microscope objective lens (Plan Apochromat 10X, Zeiss, Jena, Germany; air immersion, NA: 0.45) to a diffraction limited spot through a 170 µm thick glass slide on top of which the sample is placed (see 3.2.5 Sample preparation). For OAM detection, a spherically focused 100 MHz transducer (SONAXIS, Besancon, France; bandwidth: ~10-180 MHz, focal distance: 2.85 mm, active element diameter: 3 mm) is located in transmission mode with respect to the illumination above the sample. Acoustic coupling is provided by a water droplet between sample and transducer. The acquired optoacoustic signals are amplified by 63 dB (AU 1291, Miteq, New York, USA) and recorded by a high-speed 12-bit DAQ card (ADQ412, SP Devices, Linköping, Sweden; max. sampling rate per channel: 4 GS/s). Adjustment of the setup and alignment of both the optical and the acoustic focus co-axially to one another is achieved by two high-precision motorized xyz-stages (MLS203-2 & MZS500, Thorlabs; M-683.2U4 & M-501.1DG, Physik Instrumente GmbH & Co. KG, Karlsruhe, Germany), as described in more detail in [41]. In order to cover the scanned region of the optical beam with the acoustic sensitive field, the transducer is placed 700 µm in positive defocus with respect to the optical focus.

Both DAQ cards, and thus the acquisition as well as the movement of the GMs, are triggered by a photodiode (DET36A, Thorlabs) and thereby synchronized to the laser repetition rate. In order to generate an OAM image, a field of view (FOV) of 630 µm x 630 µm with a resolution

of 600 x 600 pixels and an averaging of 20 is recorded by step wise raster-scanning the beam across the sample. To assign the OAM signals with the corresponding position or rather pixel in the final image, the direct current (DC) coupled position feedback of the GMs is amplitude modulated by an alternating current (AC) generated by an arbitrary waveform function generator (DG1022, Rigol Technologies Inc., Beaverton, USA) to be recordable by the AC coupled high-speed DAQ card. Both the amplified time-resolved optoacoustic signals as well as the actual positions are acquired at 450 MS/s by means of a continuous multirecord (CMR) mode, a streaming-like acquisition mode in which records stored in temporary buffers on the internal memory of the DAQ card are fetched to the computer memory while acquiring the remaining records. In OAM, raw signals are bandpass filtered in the range of 10-180 MHz and their maximum amplitude is extracted to generate an unprocessed maximum amplitude projection (MAP) image. The synchronization of both DAQ cards, control of the raster-scan by means of GMs, the CMR based data acquisition, as well as filtering and projection of raw OAM signals is fully performed in Matlab (Matlab 2014a, Mathworks, Natick, USA).

3.2.3 Multiphoton microscopy (MPM)

MPM subsystem of MPOM, as comprehensively described in [40,41], employs an Yb-based solid-state laser (YBIX, Time-Bandwidth, Zurich, Switzerland; energy per pulse: 30 nJ, pulse width: 170 fs, repetition rate: 84.4 MHz) to excite the specimen at 1043 nm in order to generate NLO effects, namely SHG, THG, and TPEF. Whereas the THG signal is acquired in transmission mode, SHG and TPEF signals are acquired in backward direction after filtering out the laser excitation with a shortpass dichroic mirror (DMSP805R, Thorlabs). The NLO signals are separated using optical filters (SHG (FB520-10), THG (FGUV11), TPEF (FELH0550), Thorlabs) and are recorded by highly sensitive PMTs (H9305 03, Hamamatsu, Hamamatsu City, Japan). Digitizing is achieved by the previously mentioned 16-bit DAQ card, which is also controlling the GM scanning with a predefined scanning frequency of 320 kHz. MPM images in this work are acquired in a FOV of 630 µm x 630 µm with a resolution of 800

x 800 pixels and an averaging of 100. For the purpose of optimizing the superposition of all MPOM modalities, direction and collimation of both beams prior to entering the microscope objective lens are achieved by a shearing interferometer (SI050, Thorlabs). Chromatic deviation in z between the foci of the two laser systems are corrected by the sample holding xyz-stage. MPM image acquisition as well as controlling of both xyz-stages is carried out by LabVIEW programs [40,41].

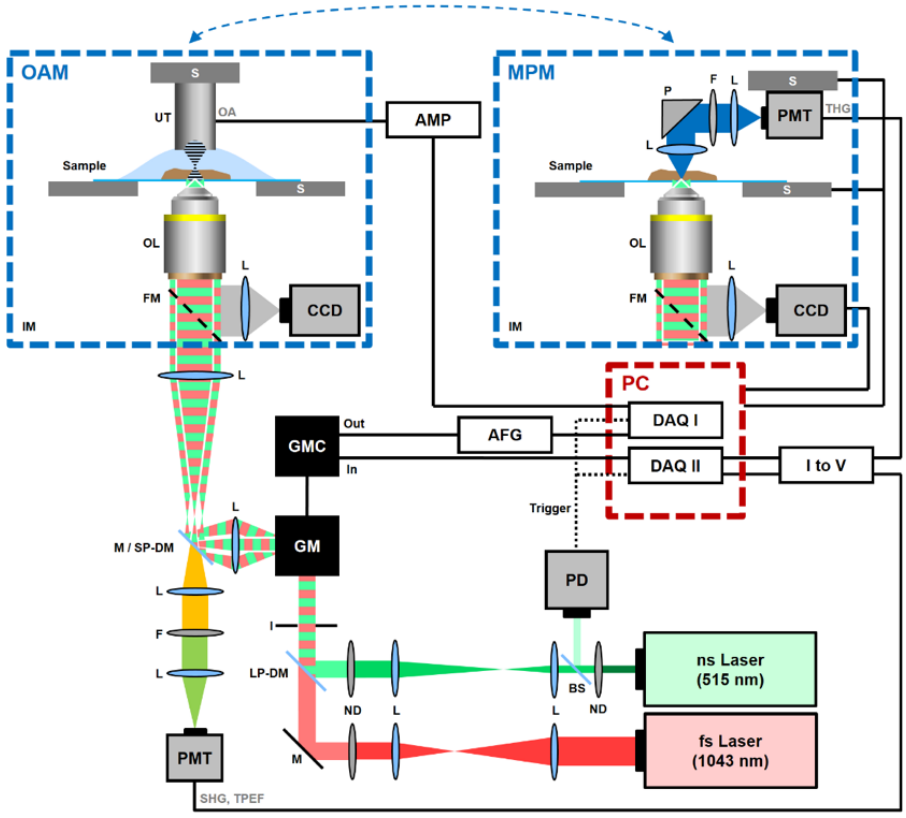

Fig. 3.1. Schematic depiction of MPOM consisting of two interchangeable microscopy systems, namely OAM and MPM. Abbreviations: AFG, arbitrary function generator; AMP, amplifier; BS, beamsplitter; DAQ, data acquisition card; F, optical filter; FM, flippable mirror; GM, galvanometric mirrors; GMC, GM control; I, iris diaphragm; L, lens; LP-DM, longpass dichroic mirror; M, mirror; ND, neutral density filter; OA, optoacoustic signal; OL, microscope objective lens; P, prism; PD, photodiode; PMT, photomultiplier tube; S, xyz-stage; SHG, second harmonic generation signal; SP-DM, shortpass dichroic mirror; UT, ultrasound transducer; THG, third harmonic generation signal; TPEF, two-photon excitation fluorescence signal. Reprinted with permission from [58].

3.2.4 Imaging protocol and image registration

Widefield BF images (Aperio CS2, Leica, Wetzlar, Germany) could be complemented by acquiring coarse optoacoustic imaging over a 10 mm x 10 mm FOV using a mechanical scan of the sample holding xyz-stage with a large step size of 100 µm. Then, specific ROIs could be selected on the large FOV images for high-resolution visualization by OAM and MPM. Prior to MPM examination, the water droplet used as acoustic coupling medium between transducer and sample for OAM imaging was removed. Image processing and co-registration of the four modalities was carried out in ImageJ (ImageJ 1.50e, Wayne Rasband). OAM and MPM images were upsampled by bicubic interpolation, median filtered, and histogram-wise adjusted to saturate 1 % of the pixels. Final co-registration of all modalities was performed by using the built-in function StackReg executing an affine transformation whereas the TPEF image was used as an "anchor" for the OAM images [43]. Through exciting the sample at two close wavelengths (TPEF: 521.5 nm; OAM: 515 nm), the corresponding obtained signals lead to partially shared information content although the signal generation differs. OAM relies on an absorption contrast, such as the one from hemoglobin stored in RBCs, whereas TPEF detects natural fluorochromes such as elastin. Nevertheless, we found that these two signatures could be accurately registered.

3.2.5 Sample preparation

A human atherosclerotic tissue sample was acquired from a patient with advanced carotid artery stenosis, who underwent carotid thrombendarterectomy (CAE). The surgically removed atherosclerotic plaque was further segmented in blocks of 3-4 mm length, fixed in formalin overnight, and subsequently embedded in paraffin. Each segment was further cut into 10 µm thick slices and the selected samples were placed on thin glass slides (170 µm) to facilitate hybrid MPOM imaging. In order to assess the plaque morphology, three different staining procedures were applied: Hemalaun-Eosin (HE) to evaluate plaque cellularity, Picro-Sirius Red (PSR) to visualize collagen fibres, and Orcein to show elastin fibres. Herein, three

different slices were chosen, which were directly adjacent to the unstained slice used for hybrid MPOM imaging within the same sample. For the validation of our methods and to demonstrate its capabilities, we present standard histological images of the approximate same positions in the sample (Aperio CS2, Leica) [44,45].

3.3 Results

First, we examined the appearance of widefield BF and coarse OAM images with respect to topological features of atherosclerotic tissue samples. Fig. 3.2a depicts a schematic subdivision of atheromas, which is sectioned into structural regions such as the lumen, the shoulders, the cap, and the core. Fig. 3.2b presents a widefield BF image of the sample. Fig. 3.2c shows a co-registered coarse OAM scan of the whole sample, obtained in the same orientation as in Fig. 3.2b. Fig. 3.2 preliminary reveals a complementarity between colour contrast seen on Fig. 3.2b and absorption contrast seen on Fig. 3.2c. In particular, a characteristic intraplaque yellow-brown pattern throughout the tissue sample, possibly due to embedded RBC residues, is also visualized as an optoacoustic pattern on Fig. 3.2c.

The coarse examination of Fig. 3.2 allows for the overall assessment of the sample regarding its global morphology, narrowing of the lumen, level of degradation, and, thus, the estimation of the degree of severity and the potential risk of rupture. Based on these coarse sample images we could then select specific plaque compartments for studying their fine local topological structure using the MPOM modalities. We selected ROIs close to the lumen in the shoulder region (ROI 1), centred at the cap (ROI 2), and in the lipid core (ROI 3).

Fig. 3.3 depicts the MPOM examination of ROI 1 close to the former lumen in the shoulder region. Fig. 3.3a presents a composite image combining OAM, SHG, THG, and TPEF images. Fig. 3.3b shows the RBC distribution imaged by OAM, Fig. 3.3c shows the collagen structure imaged by SHG, Fig. 3.3d is the BF appearance of ROI 1, Fig. 3.3e is the THG image representative of the overall cell morphology, and Fig. 3.3f shows the elastin network yielded by TPEF. The merged image (Fig. 3.3a) demonstrates no clear mutual interaction among the

components imaged and reveals an intact connective tissue. No prominent RBC clusters are present. Moreover, collagen and elastin appear largely fibrillar, ribbon shaped, and unfractured. Regarding the cell morphology, no inclusions or fissures larger than a few tens of micrometres can be seen.

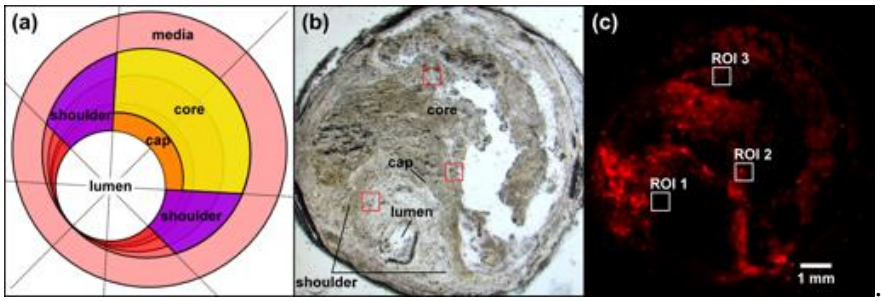

Fig. 3.2. Coarse imaging and ROI selection of human carotid atheroma. (a) Schematic depiction of a typical atherosclerotic vascular cross-section. (b) Widefield BF observation of the unstained atheroma sample used for MPOM imaging and identification of lumen, cap, and shoulders. (c) Coarse OAM scan indicating a progressed intraplaque RBC embedding. Final ROI selection for subsequent MPOM imaging is indicated by the red or white boxes. Reprinted with permission from [58].

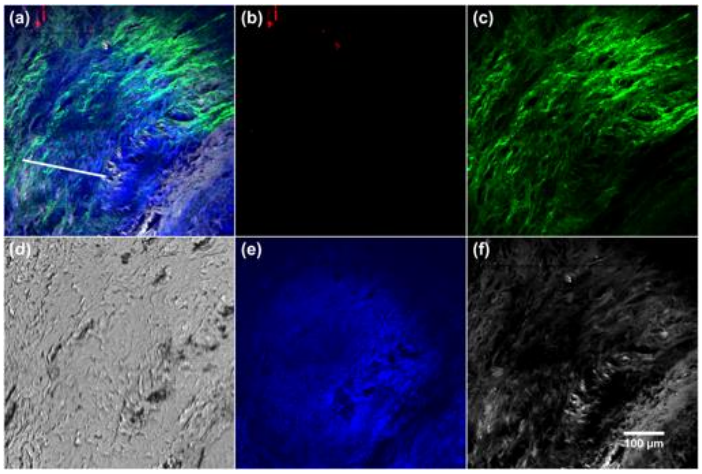

Fig. 3.3. Hybrid microscopy imaging of human carotid atheroma at the shoulder region. (a) Overlay of OA, SHG, THG, and TPEF demonstrates an unscathed condition of the connective tissue (e.g. collagen and elastin), no large inclusions or fissures, and a negligible amount of embedded blood residues. Separate depiction of (b) RBC embeddings (OAM), (c) collagen (SHG), (d) tissue appearance (BF), (e) tissue morphology (THG), and (f) mainly elastin (TPEF). Profile for subsequent analysis is indicated by the white line in (a). Reprinted with permission from [58].

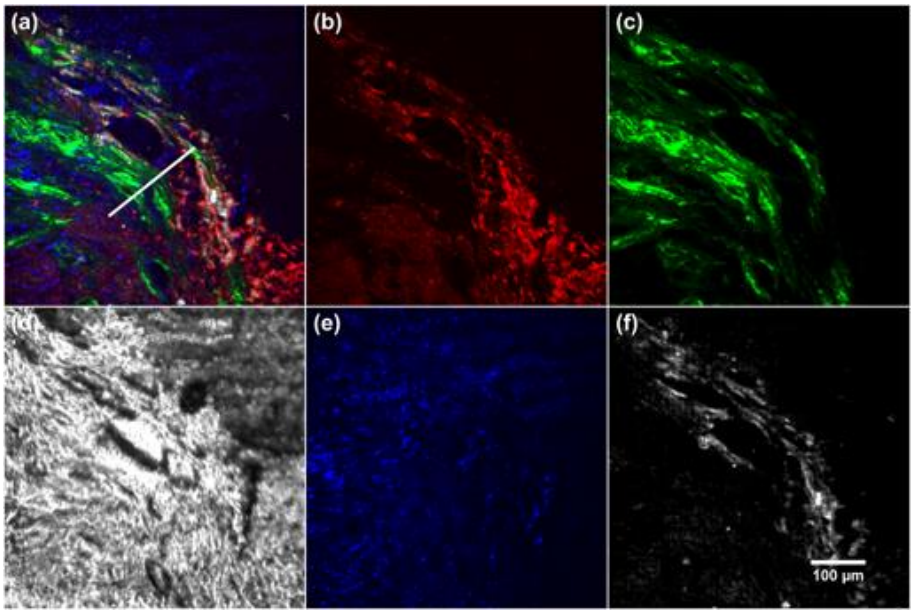

Fig. 3.4. Hybrid microscopy imaging of human carotid atheroma at the cap region. (a) Overlay of OAM, SHG, THG, and TPEF indicates coarse interleaving structure of embedded blood residues and connective tissue bands of collagen and elastin. Separate depiction of (b) RBC embeddings (OAM), (c) collagen (SHG), (d) tissue appearance (BF), (e) tissue morphology (THG), and (f) mainly elastin and RBCs (TPEF). Profile for next analysis is marked by the white line in (a). Reprinted with permission from [58].

Fig. 3.4 shows MPOM images from ROI 2. As previously, the merged image is shown in Fig. 3.4a and the OAM, SHG, BF, THG, and TPEF images are shown in Fig. 3.4b-f, respectively. Fig. 3.4a represents the merged image and exhibits marked differences compared to Fig. 3.3a. A pattern of embedded RBCs, resolved by OAM, appears co-localized with the connective tissue, i.e. collagen revealed by SHG and elastin revealed by TPEF. Furthermore, an alternating structure of RBC inclusions and connective tissue can be seen. In ROI 2 THG and BF observation reveal a slightly disturbed cell morphology including fissures and inclusions in the range of 10-100 µm.

Fig. 3.5 illustrates MPOM images of the lipid core (ROI 3), in the same order followed for Fig. 3.3 and 3.4. As obvious in the merged overlay (Fig. 3.5a), there is congruence between blood residues (OAM) and collagen fibres (SHG) in the lipid core. Embedded RBCs appear in clusters, whereby collagen fibres appear widened and split up into smaller fibrils. A fine

interleaving of these two structures can be seen. Furthermore, TPEF reveal the presence of round-shaped structures in the upper right corner, which cannot be assigned with OAM signals generally indicating blood residues. Thus, this pattern might indicate inclusions of LDL and foam cells, which are prominent in the lipid core. Finally, an advanced degradation of cell morphology can be observed.

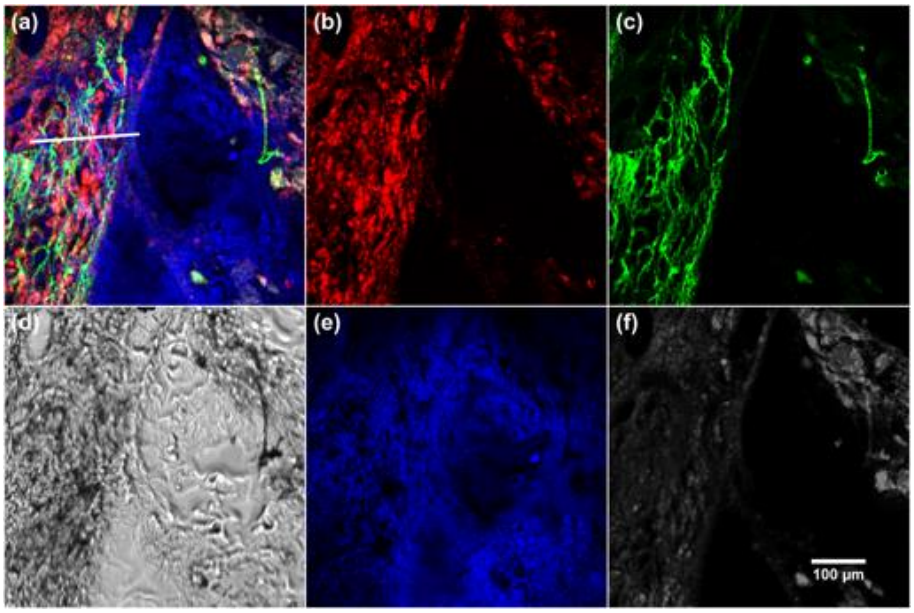

Fig. 3.5. Hybrid microscopy imaging of human carotid atheroma at the lipid core. (a) Overlay of OAM, SHG, THG, and TPEF reveals fine interleaving structure of embedded blood residues and collagen bands. Separate depiction of (b) RBC embeddings (OAM), (c) collagen (SHG), (d) tissue appearance (BF), (e) tissue morphology (THG), and (f) elastin, LDL, foam cells, and RBCs (TPEF). Profile for subsequent analysis is indicated by the white line in (a). Reprinted with permission from [58].

Fig. 6 plots the OAM, SHG, and TPEF profiles along the white lines marked in Fig. 3.3a, 3.4a and 3.5a, and allows for the observation of the spatial scale of the corresponding structures. The plots demonstrate different interleaved patterns of SHG and OAM signals at different scales depending on the observed ROI. Fig. 3.6a, obtained close to the lumen (ROI 1), confirms the lack of congruence between RBCs and collagen. The SHG profile indicates an intact collagen ribbon of at least 200 µm width consisting of individual collagen strands of 2-

10 µm diameter. In contrast, Fig. 3.6b visualizes a coarse widening of the collagen bands (ROI 2). Large gaps in the range of 80-100 µm indicate partially intact collagen ribbons interleaved with areas of embedded RBCs. Fig. 3.6c plots the most advanced interaction between RBCs and collaged recorded from the three ROIs. These interleaving structures, observed in the lipid core (ROI 3), occur in the range of 8-15 µm. Although the widths of detected collagen fibrils match the ones seen in ROI 1 (Fig. 3.6a), assumed as an unharmed collagen structure, these strands are separated from one another by incorporated RBCs.

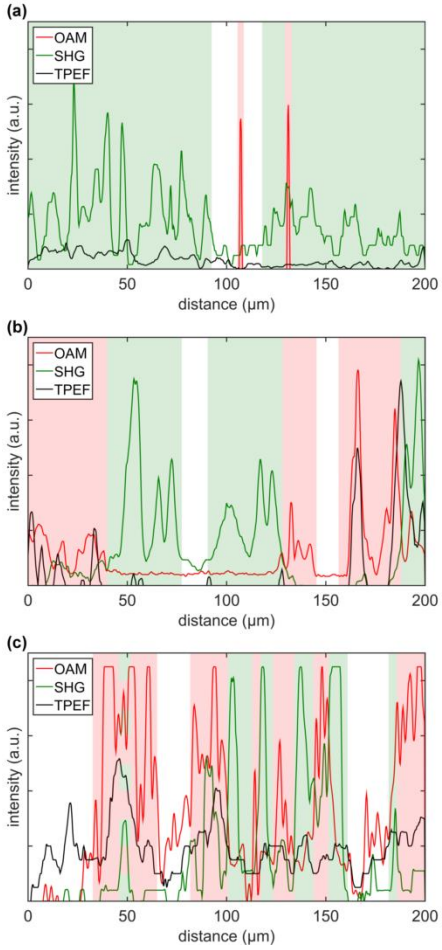

Fig. 3.6. Profiles of embedded blood residues, collagen, and elastin along the white lines indicated in Fig. 3.3a, 3.4a and 3.5a. The interleaving interaction between intraplaque coagulated RBCs and collagen occurs on different size levels leading to undisturbed collagen bands (a; ROI 1), coarse interrupted collagen stripes (b; ROI 2), and fine expanded structures (c; ROI 3). Partially shared signatures among OAM and TPEF reveal blood distribution whereas signals occurring only in TPEF present elastin within the sample. Coloured areas represent dominant compound in this region (red: RBC (OAM); green: collagen (SHG)). Reprinted with permission from [58].

In a next step we compared the MPOM findings with conventional histopathology images, acquired from approximately the same regions imaged by MPOM (Fig. 3.7). HE staining of cell nuclei, cytoplasm, and RBCs, PSR staining of collagen, and Orcein staining of elastin are depicted in the first, second, and third column of Fig. 3.7, respectively, for three specimens obtained from the shoulder (ROI 1), the cap (ROI 2), and the lipid core (ROI 3) region. Whereas at the shoulder region only single RBCs are present (Fig. 3.7a), the cap region is characterized by larger RBC inclusions (Fig. 3.7d), and the lipid core contains widely spread RBC coagulated aggregates (Fig. 3.7g). In addition, the collagen as well as the elastin structures tend to widen and expand from an unharmed and strong regular shape at the shoulder region (Fig. 3.7b,c), through an intermediate situation at the cap (Fig. 3.7e,f), to a fine subdivided distribution in the lipid core (Fig. 3.7h,i). It can be also observed that single fibrillar structures, such as collagen and elastin, cannot be unambiguously identified. These observations confirm differences in histological appearance between the three ROIs examined and complement the MPOM findings.

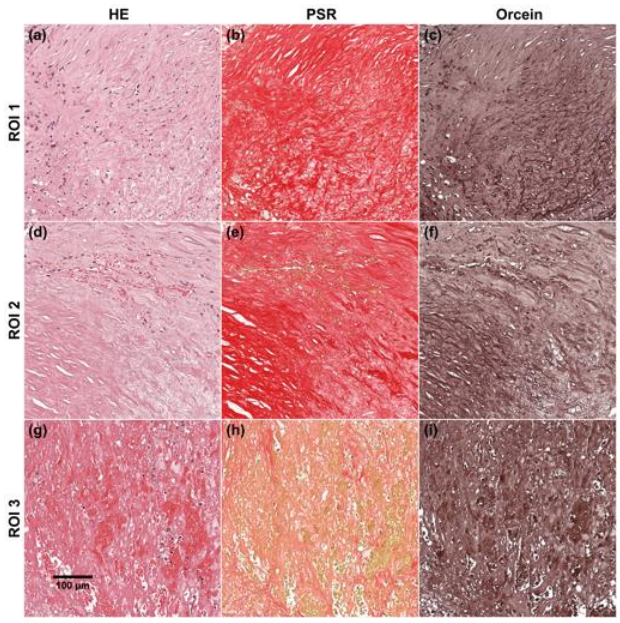

Fig. 3.7. Histological images of human carotid atheroma validating MPOM performance. (a) HE staining of cell nuclei (blue), cytoplasm (pink), and RBCs (dark red), (b) PSR staining of collagen (dark red), and (c) Orcein staining of elastin of the sample regions at the shoulder (ROI 1). Analogous depiction of (d,g) HE, (e,h) PSR, and (f,i) Orcein staining for ROI 2 and ROI 3, respectively. Reprinted with permission from [58].

3.4 Discussion

We investigated label-free visualization of human atheroma using multimodal optical and optoacoustic microscopy. Label-free imaging is researched herein as a complementary method to conventional histopathology analysis. An increasing number of label-free contrast mechanisms can thus visualize histopathologically interesting compounds such as erythrocytes, collagen, elastin, foam cells, macrophages, and the overall tissue morphology by the combination of OAM and NLO microscopy methods [40,41]. Even though OAM was implemented herein at a single wavelength, imaging at multiple wavelengths can further increase the number of labels available to the multimodal system, e.g. enabling the visualization of lipids.

The hybrid microscopy aimed at revealing different structural and morphological components of human atheroma and demonstrated the ability to co-localize readings of RBCs, elastin, collagen, lipid, and other moieties. Type I and II collagen can be imaged using SHG due to the collagen's non-centrosymmetry and birefringence properties [46–49]. Based on intrinsic autofluoresence, elastin, LDL, foam cells, and to a smaller extent embedded RBCs can be probed by TPEF [46–48], whereas THG is sensitive to the overall tissue morphology due to optical interface heterogeneities such as cell boundaries [47,50]. Finally, embedded RBCs are visualized by OAM based on the strong optical absorption of hemoglobin in the visible range in combination with a low quantum yield [51,52].

In the healthy arterial wall, which shows a viscoelastic behaviour, collagen (along with elastin) represents the elastic component and warrants vessel stability, while arterial wall viscosity is mainly reflected by the function of SMCs. According to basic studies, in the load-free wall (ex vivo), the collagen fibres seem to be corrugated. On the other side, under strong wall stresses, collagen fibrils are being elongated, reaching their elastic limit and offering enhanced mechanical strength to the arterial wall [53]. Regarding atheromatous tissue, collagen synthesis and degradation influences plaque stability and progression: Excessive collagen production may accelerate stenosis, while collagen decomposition seems to be correlated with

increased rupture susceptibility [54]. Furthermore, RBCs are thought to be a potential contributor to atheroma accumulation and progression [55]. Both neovascularization and IPH are considered as basic factors of increased plaque vulnerability [56]. From a histological point of view, the profile of a vulnerable plaque shows the following features: 1) a large lipid core, 2) a small number of SMCs, low quantity and quality of collagen within the fibrous cap, 3) enhanced accumulation of inflammatory cells (macrophages and T-lymphocytes) in the shoulder regions and the cap, and 4) the presence of neovessels and IPH [21]. According to this data, the intraplaque statuses of collagen and RBCs are critical elements of plaque vulnerability.

In the current study, we presented data visualizing collagen, elastin, and RBC congruence within a human carotid sample. MPOM reveals these moieties without the need of staining. Therefore, composite signals can be acquired from the same slice without the need to interleave and stain slices, leading to a precise topological co-registration between different signals. Further optimization of the current system could allow for the simultaneous detection of other constituents (e.g. lipids), giving a wider possibility for stain-free investigation of tissues. In the future, detailed microscopic observations of atheroma could be combined with macroscopical observations for example employing multispectral optoacoustic tomography (MSOT) [57].

3.5 References

1. WHO, The top 10 causes of death, (2013). http://who.int/mediacentre/factsheets/fs310/en/index2.html (accessed January 27, 2014).

2. W. Insull, The pathology of atherosclerosis: plaque development and plaque responses to medical treatment., Am. J. Med. 122 (2009) S3–S14. doi:10.1016/j.amjmed.2008.10.013.

3. B.C. Dickson, A.I. Gotlieb, Towards understanding acute destabilization of vulnerable atherosclerotic plaques., Cardiovasc. Pathol. 12 237–48. http://www.ncbi.nlm.nih.gov/pubmed/14507572 (accessed February 13, 2016).

4. R.B. Singh, S.A. Mengi, Y.-J. Xu, A.S. Arneja, N.S. Dhalla, Pathogenesis of atherosclerosis: A multifactorial process., Exp. Clin. Cardiol. 7 (2002) 40–53. http://www.pubmedcentral.nih.gov/articlerender.fcgi?artid=2716189&tool=pmcentrez&rendertype=abstract (accessed February 12, 2016).

5. R. Virmani, A. Burke, E. Ladich, F.D. Kolodgie, Pathology of carotid artery atherosclerotic disease, in: J. Gillard, M. Graves, T. Hatsukami, C. Yuan (Eds.), Carotid Dis. Role Imaging Diagnosis Manag., Cambridge University Press, 2007.

6. H.C. Stary, A.B. Chandler, S. Glagov, J.R. Guyton, W. Insull, M.E. Rosenfeld, S.A. Schaffer, C.J. Schwartz, W.D. Wagner, R.W. Wissler, A definition of initial, fatty streak, and intermediate lesions of atherosclerosis. A report from the Committee on Vascular Lesions of the Council on Arteriosclerosis, American Heart Association., Circulation. 89 (1994) 2462–78. http://www.ncbi.nlm.nih.gov/pubmed/8181179 (accessed February 13, 2016).

7. D. Gutstein, Pathophysiology and clinical significance of atherosclerotic plaque rupture, Cardiovasc. Res. 41 (1999) 323–333. doi:10.1016/S0008-6363(98)00322-8.

8. H.C. Stary, A.B. Chandler, R.E. Dinsmore, V. Fuster, S. Glagov, W. Insull, M.E. Rosenfeld, C.J. Schwartz, W.D. Wagner, R.W. Wissler, A Definition of Advanced Types of Atherosclerotic Lesions and a Histological Classification of Atherosclerosis : A Report From the Committee on Vascular Lesions of the Council on Arteriosclerosis, American Heart Association, Circulation. 92 (1995) 1355–1374. doi:10.1161/01.CIR.92.5.1355.

9. J.M. Mann, M.J. Davies, Vulnerable Plaque: Relation of Characteristics to Degree of Stenosis in Human Coronary Arteries, Circulation. 94 (1996) 928–931. doi:10.1161/01.CIR.94.5.928.

10. E. Falk, P.K. Shah, V. Fuster, Coronary plaque disruption., Circulation. 92 (1995) 657–71. http://www.ncbi.nlm.nih.gov/pubmed/7634481 (accessed September 7, 2014).

11. P.D. Richardson, M.J. Davies, G. V Born, Influence of plaque configuration and stress distribution on fissuring of coronary atherosclerotic plaques., Lancet (London, England). 2 (1989) 941–4. http://www.ncbi.nlm.nih.gov/pubmed/2571862 (accessed February 4, 2016).

12. G. Pasterkamp, A.H. Schoneveld, A.C. van der Wal, D.-J. Hijnen, W.J.A. van Wolveren, S. Plomp, H.L.J.M. Teepen, C. Borst, Inflammation of the Atherosclerotic Cap and Shoulder of the Plaque Is a Common and Locally Observed Feature in Unruptured Plaques of Femoral and Coronary Arteries, Arterioscler. Thromb. Vasc. Biol. 19 (1999) 54–58. doi:10.1161/01.ATV.19.1.54.

13. D.A. Chistiakov, A.N. Orekhov, Y. V Bobryshev, Contribution of neovascularization and intraplaque haemorrhage to atherosclerotic plaque progression and instability., Acta Physiol. (Oxf). 213 (2015) 539–53. doi:10.1111/apha.12438.

14. S.K. Nadkarni, B.E. Bouma, J. de Boer, G.J. Tearney, Evaluation of collagen in atherosclerotic plaques: the use of two coherent laser-based imaging methods., Lasers Med. Sci. 24 (2009) 439–45. doi:10.1007/s10103-007-0535-x.

15. J.-O. Deguchi, E. Aikawa, P. Libby, J.R. Vachon, M. Inada, S.M. Krane, P. Whittaker, M. Aikawa, Matrix metalloproteinase-13/collagenase-3 deletion promotes collagen accumulation and organization in mouse atherosclerotic plaques., Circulation. 112 (2005) 2708–15. doi:10.1161/CIRCULATIONAHA.105.562041.

16. P. Libby, M. Aikawa, Mechanisms of plaque stabilization with statins., Am. J. Cardiol. 91 (2003) 4B–8B. http://www.ncbi.nlm.nih.gov/pubmed/12615292 (accessed February 14, 2016).

17. K.-R. Purushothaman, M. Purushothaman, P. Muntner, P. a Lento, W.N. O'Connor, S.K. Sharma, V. Fuster, P.R. Moreno, Inflammation, neovascularization and intra-plaque hemorrhage are associated with increased reparative collagen content: implication for plaque progression in diabetic atherosclerosis., Vasc. Med. 16 (2011) 103–8. doi:10.1177/1358863X11402249.

18. J.F. Bentzon, F. Otsuka, R. Virmani, E. Falk, Mechanisms of Plaque Formation and Rupture, Circ. Res. 114 (2014) 1852–1866. doi:10.1161/CIRCRESAHA.114.302721.

19. R. Virmani, Atherosclerotic Plaque Progression and Vulnerability to Rupture: Angiogenesis as a Source of Intraplaque Hemorrhage, Arterioscler. Thromb. Vasc. Biol. 25 (2005) 2054–2061. doi:10.1161/01.ATV.0000178991.71605.18.

20. J. Milei, J.C. Parodi, M. Ferreira, A. Barrone, D.R. Grana, L. Matturri, Atherosclerotic plaque rupture and intraplaque hemorrhage do not correlate with symptoms in carotid artery stenosis, J. Vasc. Surg. 38 (2003) 1241–1247. doi:10.1016/S0741-5214(03)00910-8.

21. R. Virmani, F.D. Kolodgie, A.P. Burke, A. Farb, S.M. Schwartz, Lessons From Sudden Coronary Death, Arterioscler. Thromb. (2000) 1262–1275. doi:10.1161/01.ATV.20.5.1262.

22. M. Van Zandvoort, W. Engels, K. Douma, L. Beckers, M. Oude Egbrink, M. Daemen, D.W. Slaaf, Two-Photon Microscopy for Imaging of the (Atherosclerotic) Vascular Wall: A Proof of Concept Study, J. Vasc. Res. 41 (2004) 54–63. doi:10.1159/000076246.

23. S. Massberg, K. Brand, S. Gruner, S. Page, E. Muller, I. Muller, W. Bergmeier, T. Richter, M. Lorenz, I. Konrad, B. Nieswandt, M. Gawaz, A critical role of platelet adhesion in the initiation of atherosclerotic lesion formation, J. Exp. Med. 196 (2002) 887–896. doi:10.1084/jem.20012044.

24. S. Massberg, M. Gawaz, S. Gruner, V. Schulte, I. Konrad, D. Zohlnhofer, U. Heinzmann, B. Nieswandt, A Crucial Role of Glycoprotein VI for Platelet Recruitment to the Injured Arterial Wall In Vivo, J. Exp. Med. 197 (2002) 41–49. doi:10.1084/jem.20020945.

25. W. Yu, J.C. Braz, A.M. Dutton, P. Prusakov, M. Rekhter, In vivo imaging of atherosclerotic plaques in apolipoprotein E deficient mice using nonlinear microscopy., J. Biomed. Opt. 12 (2007) 054008. doi:10.1117/1.2800337.

26. H. Yoo, J.W. Kim, M. Shishkov, E. Namati, T. Morse, R. Shubochkin, J.R. McCarthy, V. Ntziachristos, B.E. Bouma, F.A. Jaffer, G.J. Tearney, Intra-arterial catheter for simultaneous microstructural and molecular imaging in vivo., Nat. Med. 17 (2011) 1680–4. doi:10.1038/nm.2555.

27. F.A. Jaffer, M.A. Calfon, A. Rosenthal, G. Mallas, R.N. Razansky, A. Mauskapf, R. Weissleder, P. Libby, V. Ntziachristos, Two-dimensional intravascular near-infrared fluorescence molecular imaging of inflammation in atherosclerosis and stent-induced vascular injury., J. Am. Coll. Cardiol. 57 (2011) 2516–26. doi:10.1016/j.jacc.2011.02.036.

28. M.A. Calfon, C. Vinegoni, V. Ntziachristos, F.A. Jaffer, Intravascular near-infrared fluorescence molecular imaging of atherosclerosis: toward coronary arterial visualization of biologically high-risk plaques., J. Biomed. Opt. 15 (2010) 011107. doi:10.1117/1.3280282.

29. C. Vinegoni, I. Botnaru, E. Aikawa, M.A. Calfon, Y. Iwamoto, E.J. Folco, V. Ntziachristos, R. Weissleder, P. Libby, F.A. Jaffer, Indocyanine green enables near-infrared fluorescence imaging of lipid-rich, inflamed atherosclerotic plaques., Sci. Transl. Med. 3 (2011) 84ra45. doi:10.1126/scitranslmed.3001577.

30. T.T. Le, I.M. Langohr, M.J. Locker, M. Sturek, J.-X. Cheng, Label-free molecular imaging of atherosclerotic lesions using multimodal nonlinear optical microscopy, Biomed. Microdevices. 12 (2009) 1–20. doi:10.1117/1.2795437.Label-free.

31. M.B. Lilledahl, O.A. Haugen, C. de Lange Davies, L.O. Svaasand, Characterization of vulnerable plaques by multiphoton microscopy., J. Biomed. Opt. 12 (2014) 044005. doi:10.1117/1.2772652.

32. L.B. Mostaço-Guidolin, M.G. Sowa, A. Ridsdale, A.F. Pegoraro, M.S.D. Smith, M.D. Hewko, E.K. Kohlenberg, B. Schattka, M. Shiomi, A. Stolow, A.C.-T. Ko, Differentiating atherosclerotic plaque burden in arterial tissues using femtosecond CARS-based multimodal nonlinear optical imaging, Biomed. Opt. Express. 1 (2010) 59–73. doi:10.1364/BOE.1.000059.

33. F. a Jaffer, M. a Calfon, A. Rosenthal, G. Mallas, R.N. Razansky, A. Mauskapf, R. Weissleder, P. Libby, V. Ntziachristos, Two-dimensional intravascular near-infrared fluorescence molecular imaging of inflammation in atherosclerosis and stent-induced vascular injury., J. Am. Coll. Cardiol. 57 (2011) 2516–26. doi:10.1016/j.jacc.2011.02.036.

34. H.-W. Wang, T.T. Le, J.-X. Cheng, Label-free Imaging of Arterial Cells and Extracellular Matrix Using a Multimodal CARS Microscope., Opt. Commun. 281 (2008) 1813–1822. doi:10.1016/j.optcom.2007.07.067.

35. H.-W. Wang, I.M. Langohr, M. Sturek, J.-X. Cheng, Imaging and quantitative analysis of atherosclerotic lesions by CARS-based multimodal nonlinear optical microscopy., Arterioscler. Thromb. Vasc. Biol. 29 (2009) 1342–8. doi:10.1161/ATVBAHA.109.189316.

36. K. Jansen, M. Wu, A.F.W. van der Steen, G. van Soest, Photoacoustic imaging of human coronary atherosclerosis in two spectral bands, Photoacoustics. 2 (2014) 12–20. doi:10.1016/j.pacs.2013.11.003.

37. A. Petrov, K.E. Wynne, M.A. Parsley, I.Y. Petrov, Y. Petrov, K.A. Ruppert, D.S. Prough, D.S. DeWitt, R.O. Esenaliev, Optoacoustic detection of intra- and extracranial hematomas in rats after blast injury, Photoacoustics. 2 (2014) 75–80. doi:10.1016/j.pacs.2014.04.001.

38. S. Sethuraman, J.H. Amirian, S.H. Litovsky, R.W. Smalling, S.Y. Emelianov, Spectroscopic intravascular photoacoustic imaging to differentiate atherosclerotic plaques., Opt. Express. 16 (2008) 3362–3367. doi:10.1364/OE.16.003362.

39. B. Wang, J.L. Su, J. Amirian, S.H. Litovsky, R. Smalling, S. Emelianov, Detection of lipid in atherosclerotic vessels using ultrasound-guided spectroscopic intravascular photoacoustic imaging., Opt. Express. 18 (2010) 4889–4897. doi:10.1364/OE.18.004889.

40. G.J. Tserevelakis, D. Soliman, M. Omar, V. Ntziachristos, Hybrid multiphoton and optoacoustic microscope., Opt. Lett. 39 (2014) 1819–22. doi:10.1364/OL.39.001819.

41. D. Soliman, G.J. Tserevelakis, M. Omar, V. Ntziachristos, Combining microscopy with mesoscopy using optical and optoacoustic label-free modes, Nat. Publ. Gr. (2015) 1–9. doi:10.1038/srep12902.

42. B. Rao, F. Soto, D. Kerschensteiner, L. V Wang, Integrated photoacoustic, confocal, and two-photon microscope., J. Biomed. Opt. 19 (2014) 36002. doi:10.1117/1.JBO.19.3.036002.

43. P. Thévenaz, U.E. Ruttimann, M. Unser, A pyramid approach to subpixel registration based on intensity, IEEE Trans. Image Process. 7 (1998) 27–41. doi:10.1109/83.650848.

44. J. Pelisek, J. Pongratz, L. Deutsch, C. Reeps, T. Stadlbauer, H.-H. Eckstein, Expression and cellular localization of metalloproteases ADAMs in high graded carotid artery lesions, Scand. J. Clin. Lab. Investig. (2012) 1–9. doi:10.3109/00365513.2012.734394.

45. J. Pelisek, G. Well, C. Reeps, M. Rudelius, A. Kuehnl, M. Culmes, H. Poppert, A. Zimmermann, H. Berger, H.-H. Eckstein, Neovascularization and angiogenic factors in advanced human carotid artery stenosis., Circ. J. 76 (2012) 1274–82. doi:10.1253/circj.CJ-11-0768.

46. A. Zoumi, A. Yeh, B.J. Tromberg, Imaging cells and extracellular matrix in vivo by using second-harmonic generation and two-photon excited fluorescence., Proc. Natl. Acad. Sci. U. S. A. 99 (2002) 11014–11019. doi:10.1073/pnas.172368799.

47. H. Segawa, M. Okuno, H. Kano, P. Leproux, V. Couderc, H. Hamaguchi, Label-free tetra-modal molecular imaging of living cells with CARS, SHG, THG and TSFG (coherent anti-Stokes Raman scattering, second harmonic generation, third harmonic generation and third-order sum frequency generation), Opt. Express. 20 (2012) 9551. doi:10.1364/OE.20.009551.

48. J. Mansfield, J. Yu, D. Attenburrow, J. Moger, U. Tirlapur, J. Urban, Z. Cui, P. Winlove, The elastin network: Its relationship with collagen and cells in articular cartilage as visualized by multiphoton microscopy, J. Anat. 215 (2009) 682–691. doi:10.1111/j.1469-7580.2009.01149.x.

49. X. Chen, O. Nadiarynkh, S. Plotnikov, P.J. Campagnola, Second harmonic generation microscopy for quantitative analysis of collagen fibrillar structure, Nat Protoc. 7 (2012) 654–669. doi:10.1038/nprot.2012.009\rnprot.2012.009 [pii].

50. B. Weigelin, G.-J. Bakker, P. Friedl, Third harmonic generation microscopy of cells and tissue organization., J. Cell Sci. c (2016) 245–255. doi:10.1242/jcs.152272.

51. J. Yao, L. V. Wang, Sensitivity of photoacoustic microscopy, Photoacoustics. 2 (2014) 87–101. doi:10.1016/j.pacs.2014.04.002.

52. V. Ntziachristos, D. Razansky, Molecular imaging by means of multispectral optoacoustic tomography (MSOT)., Chem. Rev. 110 (2010) 2783–94. doi:10.1021/cr9002566.

53. T.C. Gasser, R.W. Ogden, G.A. Holzapfel, Hyperelastic modelling of arterial layers with distributed collagen fibre orientations., J. R. Soc. Interface. 3 (2006) 15–35. doi:10.1098/rsif.2005.0073.

54. M.D. Rekhter, Collagen synthesis in atherosclerosis: too much and not enough, Cardiovasc. Res. 41 (1999) 376–384. doi:10.1016/S0008-6363(98)00321-6.

55. G. Pasterkamp, R. Virmani, The erythrocyte: a new player in atheromatous core formation., Heart. 88 (2002) 115–6. doi:10.1136/heart.88.2.115.

56. A. V Finn, R.K. Jain, Coronary Plaque Neovascularization and Hemorrhage, JACC Cardiovasc Imaging. 3 (2010) 41–44. doi:10.1016/j.jcmg.2009.11.001.

57. A. Dima, V. Ntziachristos, Non-invasive carotid imaging using optoacoustic tomography., Opt. Express. 20 (2012) 25044–57. http://www.ncbi.nlm.nih.gov/pubmed/23187270 (accessed January 21, 2016).

58. Seeger M, Karlas A, Soliman D, Pelisek J, Ntziachristos V. Multimodal optoacoustic and multiphoton microscopy of human carotid atheroma. Photoacoustics. 2016 Aug 4;4(3):102-111.